Mesenchymal Stem Cell Aggregation-Released Extracellular Vesicles Induce CD31+EMCN+ Vessels in Skin Regeneration and Improve Diabetic Wound Healing

Lu Liu, Chen-Xi Zheng, Na Zhao, Ting Zhu, Cheng-Biao Hu, Nan Zhang, Ji Chen, Kai-Chao Zhang, Sha Zhang, Jie-Xi Liu, Kai Zhang, Huan Jing, Bing-Dong Sui,* Yan Jin,* and Fang Jin*

The blood vessel system is essential for skin homeostasis and regeneration. While the heterogeneity of vascular endothelial cells has been emergingly revealed, whether a regeneration-relevant vessel subtype exists in skin remains unknown. Here, a specialized vasculature in skin featured by simultaneous CD31 and EMCN expression contributing to the regeneration process is identified, the decline of which functionally underlies the impaired angiogenesis of diabetic nonhealing wounds. Moreover, enlightened by the developmental process that mesenchymal condensation induces angiogenesis, it is demonstrated that mesenchymal stem/stromal cell aggregates (CAs) provide an efficacious therapy to enhance regrowth of CD31+EMCN+ vessels in diabetic wounds, which is surprisingly suppressed by pharmacological inhibition of extracellular vesicle (EV) release. It is further shown that CAs promote secretion of angiogenic protein-enriched EVs by proteomic analysis, which directly exert high efficacy in boosting CD31+EMCN+ vessels and treating nonhealing diabetic wounds. These results add to the current knowledge on skin vasculature and help establish feasible strategies to benefit wound healing under diabetic condition.

1. Introduction

As the largest organ in the human body, the skin acts as the first line of defense against outside environment, making it highly susceptible to traumatic or surgical injuries.[1,2] The blood vessel system that is mainly distributed in the dermis and mediates the transport of nutrients and oxygen as well as disposal of wastes, is essential for skin homeostasis maintenance and regeneration.[3] Notably, the process of wound healing involves well-orchestrated sequential phases, within which angiogenesis, the growth of new blood vessels from preexisting vasculature, has been identified as an indispensable program.[2–4] Within recent years, in addition to the common recognition of vascular classification into arteries, veins and capillaries, it has been emergingly revealed that vascular endothelial cells (ECs) are highlyg heterogeneous,

L. Liu, C.-X. Zheng, T. Zhu, N. Zhang, J. Chen, K.-C. Zhang, S. Zhang,
J.-X. Liu, K. Zhang, B.-D. Sui, Y. Jin
State Key Laboratory of Military Stomatology & National Clinical
Research Center for Oral Diseases & Shaanxi International Joint Research
Center for Oral Diseases
Center for Tissue Engineering
School of Stomatology
The Fourth Military Medical University
Xi'an, Shaanxi 710032, China
E-mail: bingdong@fmmu.edu.cn; yanjin@fmmu.edu.cn
L. Liu, F. Jin
Department of Orthodontics
School of Stomatology
The Fourth Military Medical University
Xi'an, Shaanxi 710032, China
E-mail: jinfang@fmmu.edu.cn

C.-X. Zheng
Department of Oral Histopathology
School of Stomatology
The Fourth Military Medical University
Xi'an, Shaanxi 710032, China
N. Zhao, C.-B. Hu
Xi'an Key Laboratory of Stem Cell and Regenerative Medicine
Institute of Medical Research
Northwestern Polytechnical University
Xi'an, Shaanxi 710072, China
T. Zhu
Department of Preventive Dentistry
School of Stomatology
The Fourth Military Medical University
Xi'an, Shaanxi 710032, China
T. Zhu
College of Life Science
Northwest University
Xi'an, Shaanxi 710069, China
J. Chen
Department of Oral Implantology
School of Stomatology
The Fourth Military Medical University
Xi'an, Shaanxi 710032, China

constituting distinct vessel subtypes.[5,6] For example, the subtype of H vessels (CD31hiEMCNhi vessels), which was first discovered in bone, promote vascularization and couple with osteogenesis.[7] CD31 molecules are evenly distributed over the plasma membrane of blood flowing leukocytes and platelets and are concentrated at the intercellular endothelial junctions, which maintain junctional integrity of ECs and vascular permeability.[8,9] Endomucin (EMCN) is an endothelial transmembrane protein and an EC-specific sialomucin found in venous and capillaries endothelium, but not on arterial endothelium and the high endothelial venules of peripheral and mesenteric lymph nodes.[10,11] Genomic profiling techniques, in particular single-cell RNA sequencing, have depicted a detailed transcriptional atlas of skin ECs, which helps to provide more insights into the intercellular heterogeneity.[12–14] Nevertheless, the identification of specific vessel subtype in skin that is functionally associated with the regeneration process remains to be further elucidated.

Despite that minor injuries usually heal well in healthy individuals, nonhealing wounds have become a major burden worldwide in both human health and economic terms.[15] In particular, patients with diabetes are highly vulnerable to abnormal wound repair.[16,17] Of note, the impaired ability to regrow vasculature through angiogenesis is a major aspect of diabetes-related nonhealing wounds, with significantly decreased pro-angiogenic signals putatively attributed to the hyperglycemic environment and excessive proinflammatory factors.[18–21] For now, researches on the techniques and dressings used for improving angiogenesis mainly focus on delivery of angiogenic growth factors or application of small molecules, as we also previously did by testing metformin and resveratrol.[18,22–25] Despite the benefits to angiogenesis and wound closure in animal studies by these approaches, barely no reagent exerts clear therapeutic effects on enhancing angiogenesis for patients with diabetic nonhealing wounds in clinical trials.[22,26,27] Further exploration on the involvement of regeneration-relevant vessel subtype in skin will shed light on novel targets for establishing feasible therapeutics to promote nonhealing wound regeneration under diabetic conditions.

A promising regenerative paradigm currently being established is to harness or recapitulate the developmental program for organ regeneration.[28–30] Specifically, condensation of mesenchymal progenitors has been revealed as a necessary component for the development of a spectrum of organs, which not only dictates mesenchymal tissue formation and patterning, but also acts importantly as the signaling niche to orchestrate fate specification of cross-lineage progenitors and coordinate vascularization.[31–33] A typical example is the centrality of the condensing mesenchyme in regulating vascular patterning during limb development.[34] Accordingly, a great amount of efforts has been devoted into the construction and application of mesenchymal condensation mimetics for regenerative aims.[35–37] In this aspect, our group has previously constructed cell aggregates (CAs) from cultured mesenchymal stem/stromal cells (MSCs) and successfully regenerated dental pulp and periodontal bone in preclinical studies and in human clinical trials, which demonstrated abundant vascularization ascribed to paracrine effects based on release of extracellular vesicles (EVs).[38–41] The MSC-CAs we established belong to a tissue engineering product, which are based on cell sheet engineering and pellet culture technology.[40,42] This technology enables cells to be fully connected under the induction of special media, with secreting ample amount of extracellular matrix (ECM), EVs and growth factors beneficial for the cell survival, differentiation and regeneration potential.[40,42] CAs can be easily peeled off from the bottom of the cell culture dish, which avoids cell loss caused by enzymatic digestion and maximizes the preservation of cell-to-cell and cell–ECM interaction.[40,42] Nevertheless, whether MSC-CAs could regrow regenerative skin vessel subtype and show therapeutic efficacy for diabetic nonhealing wounds, as well as the underlying mechanisms, remains to be uncovered.

In this study, we first identify a specific vessel subtype featured by simultaneous CD31 and EMCN expression which preferably resides in the deep reticular layer of dermis and is phenotypically involved in wound healing via neovascularization and support of adjacent proliferating cells. Next, we show that the density of this vasculature is significantly reduced in skin of type 2 diabetes (T2D) mice and its angiogenesis is severely impaired in diabetic wound healing, with cellular and molecular investigations indicating the hyperglycemic environment diminished the CD31+EMCN+ vessel formation. Subsequently, we demonstrate that the application of MSC-CAs provides an efficacious therapy for diabetic wound healing and enhances regrowth of CD31+EMCN+ vessels, which is suppressed by pharmacological inhibition of EV release. We further show that CAs promote secretion of angiogenic protein-enriched EVs by proteomic analysis, which demonstrate high efficacy in boosting CD31+EMCN+ vessels and treating nonhealing diabetic wounds. These findings contribute to building a functional framework that CD31+EMCN+ vessels have close correlation with skin homeostasis and more importantly, the regeneration process, which further help to establish effective strategies to promote nonhealing wounds under T2D condition.

2. Results

2.1. Identification of a Specialized Blood Vessel Subtype in Skin Regeneration

To investigate the potential specialized vasculature in skin, in the beginning of this study, we particularly explored the distribution

K.-C. Zhang, Y. Jin
Xi'an Institute of Tissue Engineering and Regenerative Medicine
Xi'an, Shaanxi 710032, China
S. Zhang
Department of Traditional Chinese Medicine
Xijing Hospital
The Fourth Military Medical University
Xi'an, Shaanxi 710032, China
K. Zhang
Department of Oral and Maxillofacial Surgery
School of Stomatology
The Fourth Military Medical University
Xi'an, Shaanxi 710032, China
H. Jing
Department of Endodontics
Guangdong Provincial High-level Clinical Key Specialty
Guangdong Province Engineering Research Center of Oral Disease
Diagnosis and Treatment
Peking University Shenzhen Hospital
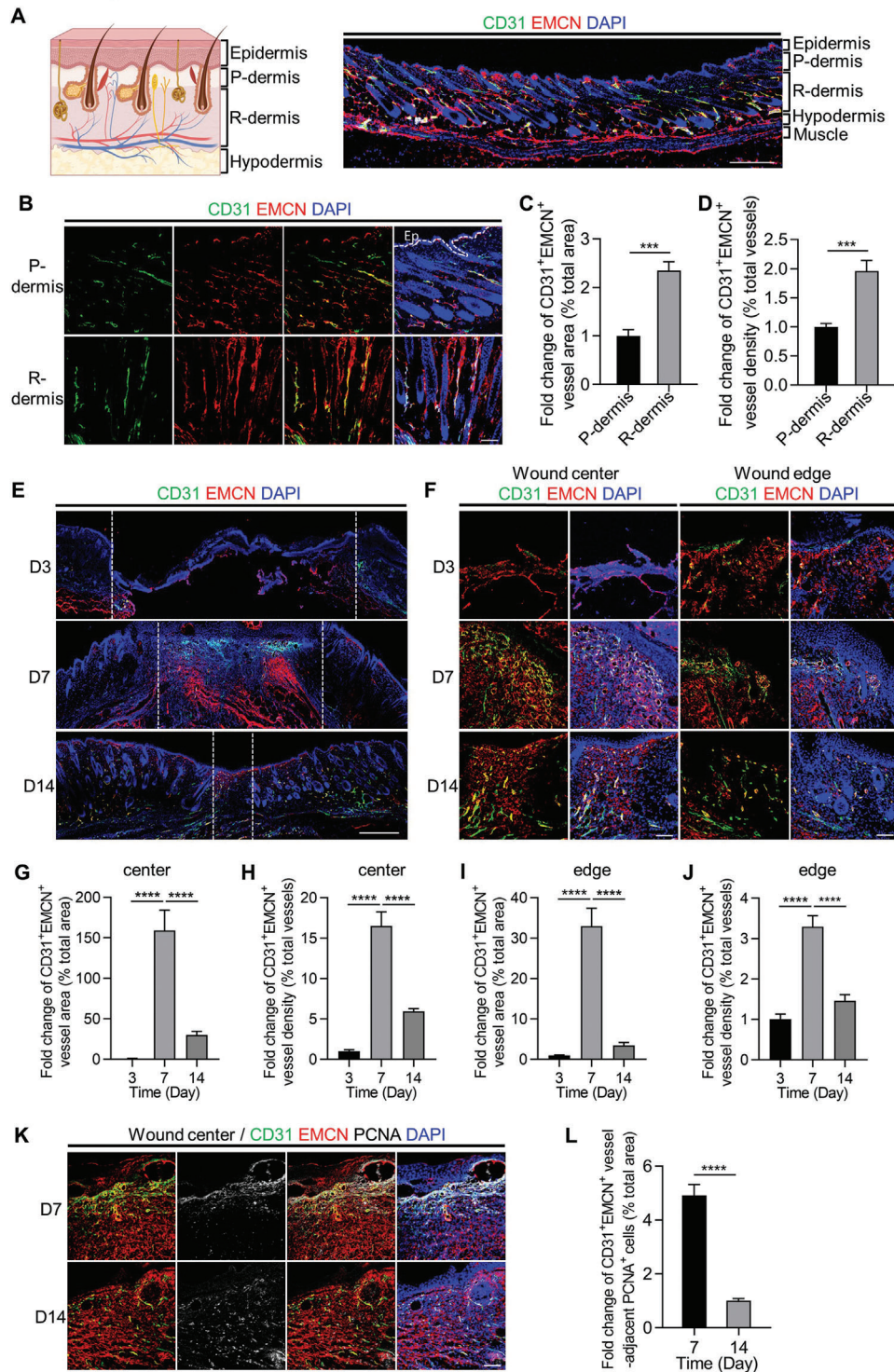Shenzhen, Guangdong 518036, China

Figure 1. Identification of a regeneration-relevant vessel subtype in skin. A) Schematic diagram of mouse skin structure, and CD31 (green) and endo-mucin (EMCN) (red) co-immunostaining in normal mouse skin, counterstained by DAPI (blue). Scale bar, 1 mm. B) CD31 (green) and EMCN (red) co-immunostaining in the papillary layer and reticular layer of dermis (P-dermis and R-dermis) in normal mouse skin, counterstained by DAPI (blue). Dotted lines outline the boundary between epidermis and dermis. Scale bar, 100 µm. C) Quantification of fold change of CD31$^+$EMCN$^+$ vessel area (% total area) in the P-dermis and R-dermis. D) Quantification of fold change of CD31$^+$EMCN$^+$ vessel density (% total vessels) in the P-dermis and R-dermis. E) The low-magnified images of CD31 (green) and EMCN (red) co-immunostaining in the wounded skin of mice at D3, D7, and D14 post-wound modeling, counterstained by DAPI (blue). Scale bar, 1 mm. F) The high-magnified images of CD31 (green) and EMCN (red) co-immunostaining in the wounded skin of mice at D3, D7, and D14 post-wound modeling, counterstained by DAPI (blue). Scale bars, 100 µm. G,H) Quantification of fold change of CD31$^+$EMCN$^+$ vessel area (% total area) and the fold change of CD31$^+$EMCN$^+$ vessel density (% total vessels), respectively, at the wound center

**ADVANCED
SCIENCE NEWS**

www.advancedsciencenews.com

**ADVANCED
HEALTHCARE
MATERIALS**

www.advhealthmat.de

of CD31$^+$EMCN$^+$ vessels and observed preferential location in the dermis layer (**Figure 1**A). The assessment methods we used and different types of vessels identified in the skin were particularly demonstrated (Figure S1A,B, Supporting Information). Further exploration demonstrated that CD31$^+$EMCN$^+$ vessels preferably resided in the deep reticular area of dermis compared to the super papillary area (Figure 1B). Quantification analysis also confirmed that both the density of CD31$^+$EMCN$^+$ vessels and the percentage of CD31$^+$EMCN$^+$ vessels within total vessels (CD31$^+$ vessels plus EMCN$^+$ vessels) were higher in the deep area of skin (Figure 1C,D), together with more CD31$^-$EMCN$^+$ vessels but less CD31$^+$EMCN$^-$ vessels in reticular dermis (R-dermis) than papillary dermis (P-dermis) (Figure S1C, Supporting Information). Next, we investigated the changes of CD31$^+$EMCN$^+$ vessels during the postnatal development process. We discovered that there were more CD31$^+$EMCN$^+$ vessels, but not CD31$^-$EMCN$^+$ and CD31$^+$EMCN$^-$ vessels, in infant (one week old) individuals compared with adult (10 weeks old) compartments (Figure S1D–G, Supporting Information), suggesting phenotypical involvement of CD31$^+$EMCN$^+$ vessels in the postnatal skin growth. In order to explore whether this vessel subtype is regeneration-relevant, we adopted the typical cutaneous wound healing model in the normal skin and performed a time course observation for the changes of CD31$^+$EMCN$^+$ vessels, according to previous reports.[43] Results showed that in the inflammation stage (D3) after wound modeling, a small number of CD31$^+$EMCN$^+$ vessels appeared in both the wound center and edge areas, and at the proliferation stage (D7), there were abundant CD31$^+$EMCN$^+$ vessels in both areas (Figure 1E–J). Notably, at the remodeling stage (D14), the number of CD31$^+$EMCN$^+$ vessels declined (Figure 1E–J). Statistical analysis confirmed the morphological observation, which is consistent with the trend of angiogenesis activity across the wound healing process, as previously reported.[18,44] In addition, during the wound healing, the changes of the proportion of CD31$^+$EMCN$^+$ vessels were more relevant and significant than the proportions of CD31$^+$EMCN$^-$ and CD31$^-$EMCN$^+$ vessels (Figure S1H,I, Supporting Information). These results indicated that CD31$^+$EMCN$^+$ vessels represent a regeneration-correlated functional vessel subtype involved in the angiogenesis process, particularly in the proliferation stage of wound healing. Accordingly, we detected preferential adjacency of proliferative cells, as marked by proliferating cell nuclear antigen (PCNA), to CD31$^+$EMCN$^+$ vessels in both wound center and edge areas, which significantly decreased in D14 compared to D7 (Figure 1K,L, and Figure S1J,K, Supporting Information). Given that cell proliferation plays a pivotal role in tissue regeneration, which depends on the oxygen and nutrition provided by vessels, our findings indicated that CD31$^+$EMCN$^+$ vessels constitute a pro-regenerative microenvironment supporting the cellular renewal during wound healing. These data collectively suggested that CD31$^+$EMCN$^+$ vessels represent a specific vascular subtype phenotypically and functionally involved in skin regeneration.

2.2. Impairment of Skin CD31$^+$EMCN$^+$ Vessels in Diabetic Wound Healing

Given that diabetes is a major systemic disease contributing to impaired wound healing, in which microvascular dysfunction acts as a key contributor,[17] we next investigated the involvement of CD31$^+$EMCN$^+$ vessels under pathological conditions by exploring the effects of diabetes on them. For this purpose, we first introduced genetically induced leptin receptor-deficient T2D db/db mice and confirmed their metabolic phenotype, as shown by overweight, high blood glucose as well as impaired glucose tolerance and insulin sensitivity (Figure S2A–D, Supporting Information). As for the histological structure of skin, hematoxylin and eosin (H&E) and Masson staining demonstrated that the skin of adult db/db mice is different from that of control db/m mice, with thinner dermis and thicker subcutaneous fat as well as significantly reduced hair follicles and collagen deposition (Figure S2E–H, Supporting Information). Notably, the density of CD31$^+$EMCN$^+$ vessels and the percentage of CD31$^+$EMCN$^+$ vessels within total vessels were much lower in db/db mice (Figure S2I–L, Supporting Information), together with reduced CD31$^-$EMCN$^+$ vessels but not CD31$^+$EMCN$^-$ vessels (Figure S2M, Supporting Information), indicating that the establishment and maintenance of functional specialized vasculature is impaired in T2D. Moreover, we performed wound healing model in db/db mice and monitored the wound area at various time points. Results demonstrated that the wound closure rate was indeed significantly inhibited in the db/db mice (**Figure 2**A,B), which was consistent with previous reports.[45] Histological staining of wound center and edge areas showed that there was only a small wounded area remaining in the control mice with the original defects covered by regenerated tissue, while the damaged area left was much larger in db/db mice (Figure S3A,B, Supporting Information). Besides, the regenerated tissue of control mice is well-organized and stratified with massive collagen deposition, enhanced formation of hair follicles, sebaceous glands and sweat glands, which was rarely observed in the db/db mice (Figure S3A–E, Supporting Information). As to the angiogenesis of CD31$^+$EMCN$^+$ vessels, we found that at D7, there was much less CD31$^+$EMCN$^+$ vessels in both wound center and edge areas of db/db mice compared to db/m mice (Figure 2C–E, Supporting Information), while CD31$^+$EMCN$^+$ vessels were still impaired in the wound center areas of db/db mice at D14 (Figure 2C,D,F). Further quantification revealed that while in normal mice, CD31$^+$EMCN$^+$ vessels significantly increased at D7 and then declined at D14, the appearance of CD31$^+$EMCN$^+$ vessels was delayed in db/db mice, although not fully blocked in our experimental condition (Figure 2G,H). Thus, the growth of CD31$^+$EMCN$^+$ vessels was suppressed in the diabetic condition, which might underlie the impaired wound healing. Further quantification of the proportions of different vascular subtypes collectively indicated that the changes of CD31$^+$EMCN$^+$

area. I,J) Quantification of fold change of CD31$^+$EMCN$^+$ vessel area (% total area) and CD31$^+$EMCN$^+$ vessel density (% total vessels), respectively, at the wound edge area. K) CD31 (green), EMCN (red), and PCNA (white) co-immunostaining at the wound center area at D7 and D14 post-wound modeling, counterstained by DAPI (blue). Scale bar, 100 μm. L) Quantification of fold change of PCNA$^+$ cells adjacent to CD31$^+$EMCN$^+$ vessels (% total area) at the wound center area at D7 and D14 post-wound modeling. Some figure elements were created with BioRender.com (accessed on November 25, 2022). $n = 3$ per group. Data are presented as mean ± SD. ***$P < 0.001$; ****$P < 0.0001$.
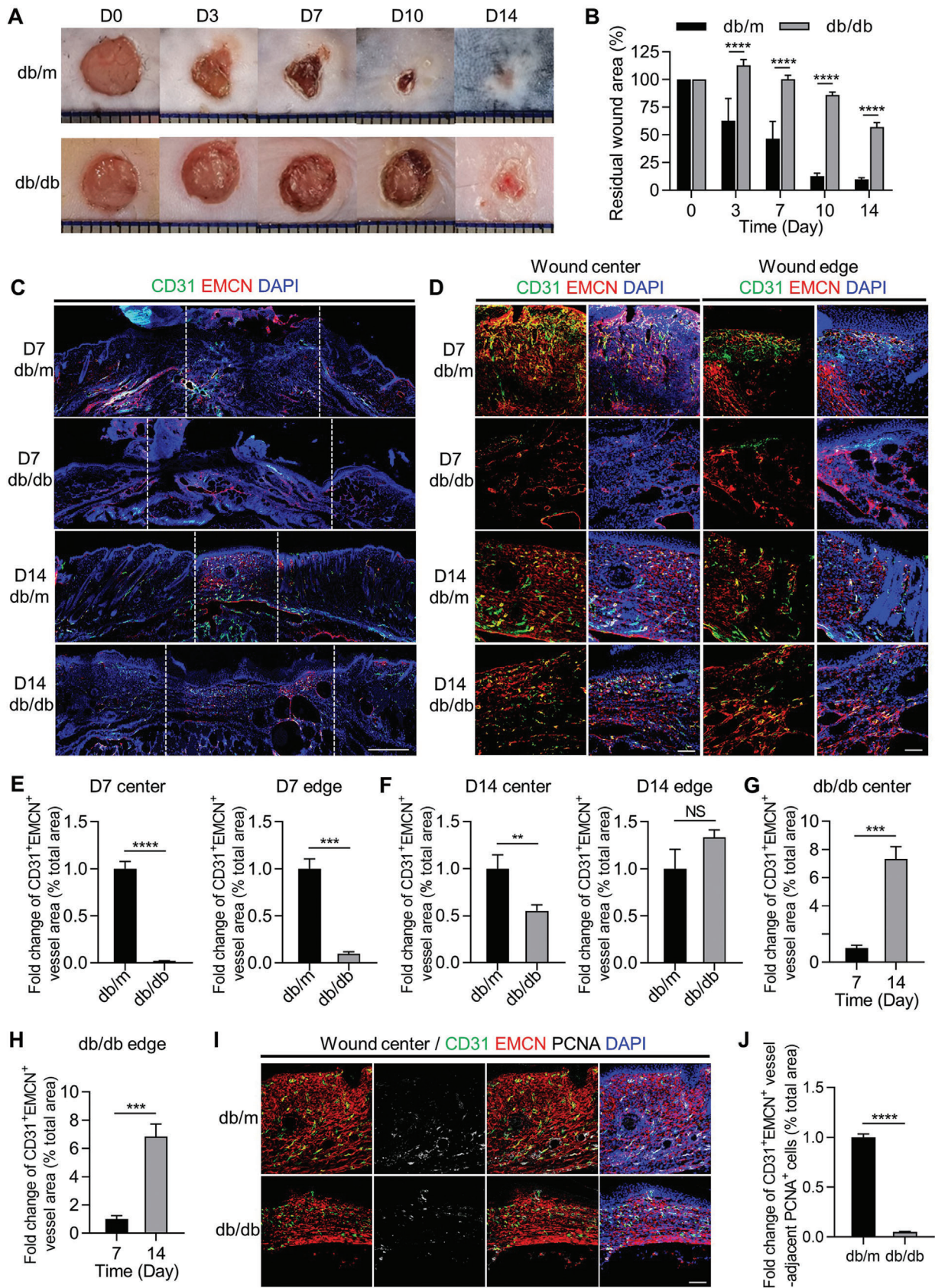
vessels were relevant and significant during the wound healing of db/db mice (Figure S3F–K, Supporting Information). Furthermore, the number of PCNA$^+$ cells adjacent to CD31$^+$EMCN$^+$ vessels was significantly lower in db/db mice than control mice in both wound center and edge areas, indicating less supporting effects for cellular proliferation (Figure 2I,J, and Figure S3L,M, Supporting Information). Collectively, these results suggested that CD31$^+$EMCN$^+$ vessels are impaired in diabetes under both normal and regenerative conditions, thus providing a potential pathogenesis.

2.3. Diminish of CD31$^+$EMCN$^+$ Vessel Formation by the Hyperglycemic Environment

Since we have shown the effects of diabetes on skin CD31$^+$EMCN$^+$ vessels, we further examined the impact of high glucose and advanced glycation end products (AGEs), namely, glycated proteins or lipids that are prevalent in the hyperglycemic environment,[46,47] on the functions of ECs. First, we performed migration and tube formation assay on human umbilical vein ECs (HUVECs) to evaluate the angiogenic capacity. Results showed that high glucose treatment significantly impaired the migration and tube formation ability of HUVECs, which was not due to the changes of osmotic pressure since the addition of mannose as the osmotic control had no effects (**Figure 3**A,C, Supporting Information). Also, the addition of AGEs demonstrated similar results (Figure 3B,D). Further quantification analysis confirmed the above observation (Figure 3E–H). Next, we used immunofluorescence staining to explore the formation of CD31$^+$EMCN$^+$ vessels in vitro. As expected, the positive staining of CD31 and EMCN as well as their co-immunostaining was dramatically decreased by high glucose and AGE treatments, consistent with in vivo findings of suppressed CD31$^+$EMCN$^+$ vessels in the diabetic skin (Figure 3I–L). Notably, we found that not all HUVECs expressed CD31 or EMCN, indicating that HUVECs might have differentiated into different directions, which was also related to the heterogeneity of HUVECs reported in the reference.[13] We analyzed the proportion of various vessels after tube formation under normal conditions and found that CD31$^-$EMCN$^+$ vessels accounted for the highest proportion, reaching about 70%, while the proportions of CD31$^+$EMCN$^+$ and CD31$^+$EMCN$^-$ were relatively low, which had no statistical difference (Figure S4A, Supporting Information). This result was consistent with the normal skin of db/m mice without injury. The Notch pathway has been reported to promote angiogenesis and contribute to the generation of CD31$^+$EMCN$^+$ type H vessels in bone.[48] In this regard, we explored the changes of the Notch1 intracellular domain (NICD) expression and found that both high glucose and AGE treatments led to dramatic decrease of NICD protein (Figure 3M–O), suggesting that inhibited Notch signaling might underlie the impairment of CD31$^+$EMCN$^+$ vessel formation in the hyperglycemic environment.

2.4. Enhancement of CD31$^+$EMCN$^+$ Vessel Regrowth and Alleviation of Diabetic Wound Healing by MSC-CAs

In this part, from a therapeutic perspective, we investigated the effects of MSC-derived CAs on diabetic refractory wounds based on our experience in engineering mesenchymal condensation-mimetics for regenerative use,[38,39] and further explored whether they could renovate impaired angiogenesis of CD31$^+$EMCN$^+$ vessels in skin. First, we constructed and characterized CAs from umbilical cord MSCs (UCMSCs). Microscopic observation showed dense lamellar structure with cells interlaced to form a woven pattern (Figure S5A, Supporting Information), and general observation showed that mature CAs could be detached from the culture plates and formed white thick membrane-condensed globular structures (Figure S5B, Supporting Information). Besides, H&E staining demonstrated that CAs were composed of multiple layers of cells forming laminated structures with abundance of extracellular matrix (ECM) (Figure S5C, Supporting Information), and scanning electron microscope (SEM) observation showed that the surface of CAs was uneven, with abundant ECM as well as multiple extra-cytoplasmic matrix vesicles attached (Figure S5D, Supporting Information). Then, CAs were applied to the wound area of db/db mice on the operation day with PBS as blank control, and the wound area was photographed at various time points (**Figure 4**A). Compared to the PBS group, CA treatment significantly accelerated the wound closure rate (Figure 4B). Histological analysis of the dissected skin tissues via H&E and Masson staining further showed that CAs treatment remarkably enhanced skin healing (Figure S5E,F, Supporting Information). On the one hand, the defect area in the CA group was closed to a much larger extent than PBS group (Figure S5E,F, Supporting Information). On the other hand, the regenerated tissue in the wound center of CA group was well-organized and stratified, with normal thickness, massive collagen deposition and increased hair follicle formation, which was rarely observed in the PBS group (Figure S5G–I, Supporting Information). The above results indicated that MSC-derived CAs possess potent therapeutic effects for diabetic skin wounds. More importantly,

Figure 2. Impairment of CD31$^+$EMCN$^+$ vessels in diabetic wounds. A) Representative photographs of full-thickness cutaneous wounds in control (db/m) and diabetic (db/db) mice, and B) quantification of the residual wound area in each group, $n = 8$ per group. C) The low-magnified images of CD31 (green) and EMCN (red) co-immunostaining in the wounded skin of db/m and db/db mice at D7 and D14 post-wound modeling, counterstained by DAPI (blue). Scale bar, 1 mm. D) The high-magnified images of CD31 (green) and EMCN (red) co-immunostaining in the wounded skin of db/m and db/db mice at D7 and D14 post-wound modeling, counterstained by DAPI (blue). Scale bars, 100 µm. E) Quantification of fold changes of CD31$^+$EMCN$^+$ vessel area (% total area) at the wound center and edge area of db/m and db/db mice at D7 post-wound modeling. F) Quantification of fold changes of CD31$^+$EMCN$^+$ vessel area (% total area) at the wound center and edge area of db/m and db/db mice at D14 post-wound modeling. G) Quantification of fold change of CD31$^+$EMCN$^+$ vessel area (% total area) at the wound center area of db/db mice at D7 and D14 post-wound modeling. H) Quantification of fold change of CD31$^+$EMCN$^+$ vessel area (% total area) at the wound edge area of db/db mice at D7 and D14 post-wound modeling. I) CD31 (green), EMCN (red) and PCNA (white) co-immunostaining at the wound center area of db/m and db/db mice at D14 post-wound modeling, counterstained by DAPI (blue). Scale bar, 100 µm. J) Quantification of fold change of PCNA$^+$ cells adjacent to CD31$^+$EMCN$^+$ vessels (% total area) at the wound center area of db/m and db/db mice at D14 post-wound modeling. $n = 3$ per group. Data are presented as mean ± SD. **$P < 0.01$; ***$P < 0.001$; ****$P < 0.0001$; NS, not significant.
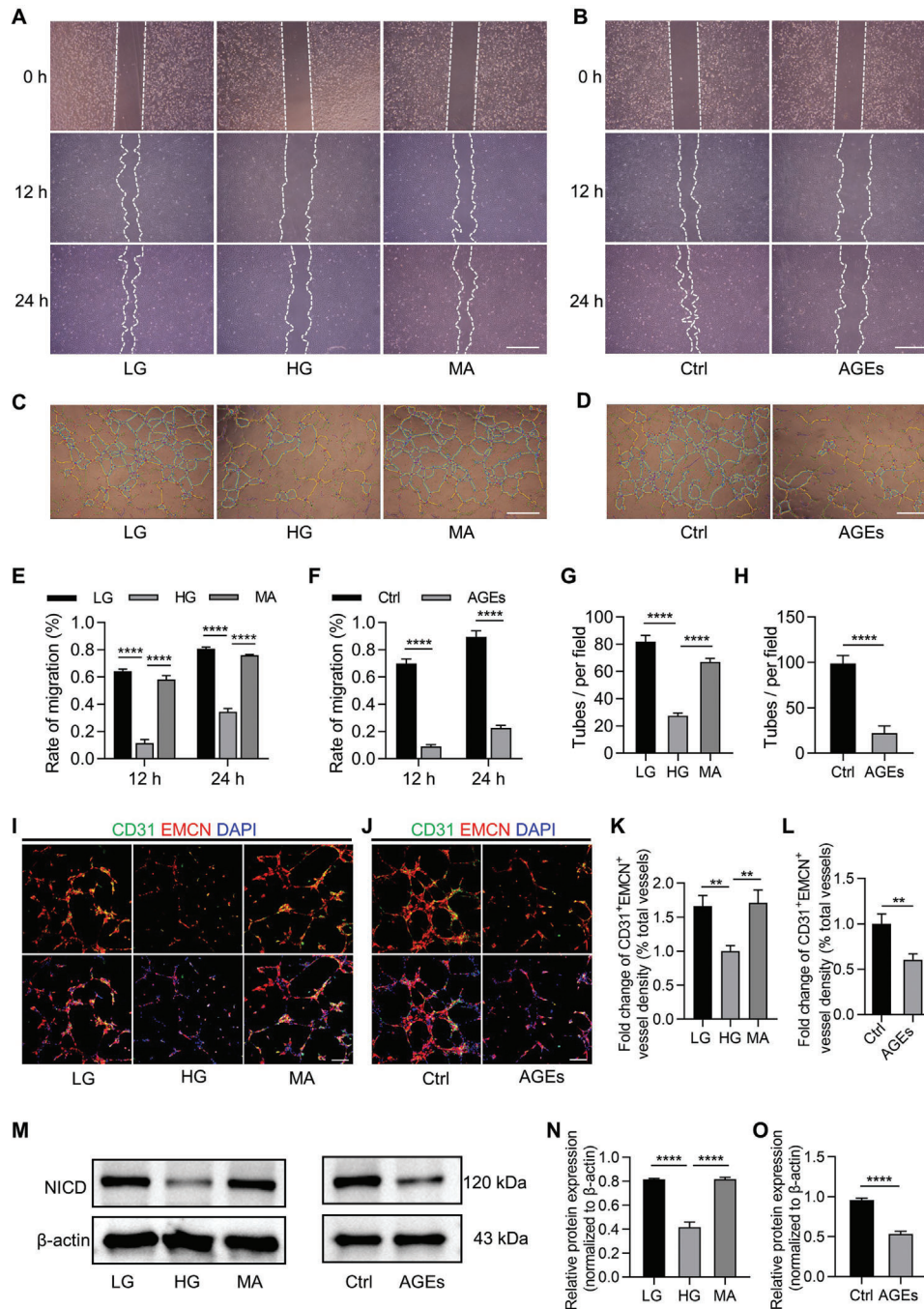
Figure 3. Impairment of CD31$^+$EMCN$^+$ vessel formation by high glucose (HG) and advanced glycation end products (AGEs). A) Representative images of scratch assay of HUVECs treated by low glucose (LG), HG, and mannitol (MA) at indicated timepoints. Scale bar, 500 µm. B) Representative images of scratch assay of HUVECs treated by PBS and AGEs at indicated timepoints. Scale bar, 500 µm. C) Representative images of tube formation assay of HUVECs treated by LG, HG, and MA. Scale bar, 500 µm. D) Representative images of tube formation assay of HUVECs treated by PBS and AGEs. Scale bar, 500 µm. E) Quantification of migration rate of HUVECs in (A). F) Quantification of migration rate of HUVECs in (B). $n = 5$ per group. G) Quantification of formed tubes of HUVECs in (C), as indicated by blue circles. H) Quantification of formed tubes of HUVECs in (D), as indicated by blue circles. $n = 4$ per group. I) CD31 (green) and EMCN (red) co-immunostaining of HUVECs in (C), counterstained by DAPI (blue). Scale bar, 100 µm. J) CD31 (green) and EMCN (red) co-immunostaining of HUVECs in (D), counterstained by DAPI (blue). Scale bar, 100 µm. K) Quantification of CD31$^+$EMCN$^+$ vessel density (% total vessels) in (I). L) Quantification of CD31$^+$EMCN$^+$ vessel density (% total vessels) in (J). M) Western blotting analysis of NICD protein in HUVECs. N,O) Quantification of the protein expression level of NICD, normalized to β-actin. $n = 3$ per group. Data are presented as mean ± SD. $**P < 0.01$; $****P < 0.0001$.
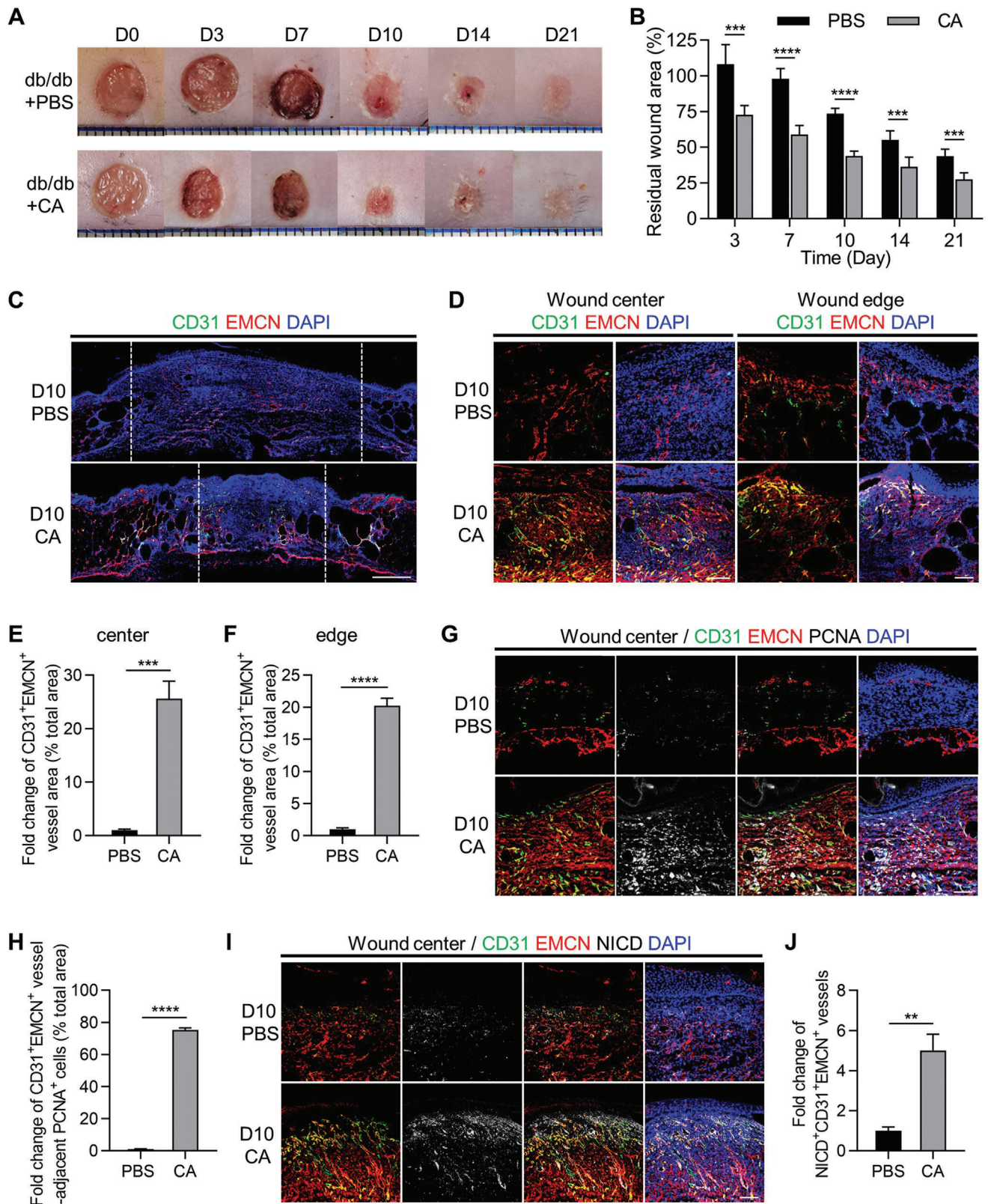
Figure 4. Enhancement of CD31$^+$EMCN$^+$ vessel regrowth and alleviation of diabetic wound healing by mesenchymal stem/stromal cell (MSC)-derived cell aggregates (CAs). AB) Representative photographs of full-thickness cutaneous wounds in PBS (control) and CA treatment groups, and B) quantification of the residual wound area in each group. $n = 6$ per group. C) The low-magnified images of CD31 (green) and EMCN (red) co-immunostaining in the wounded skin of PBS and CA groups at D10 post-treatment, counterstained by DAPI (blue). Scale bar, 1 mm. D) The high-magnified images of CD31

ADVANCED
SCIENCE NEWS

www.advancedsciencenews.com

ADVANCED
HEALTHCARE
MATERIALS

www.advhealthmat.de

after 10 d of treatment, the immunofluorescence co-staining of CD31 and EMCN showed that CAs significantly increased CD31$^+$EMCN$^+$ vessels in both the wound center and edge areas of diabetic wounds (Figure 4C,D), as confirmed by quantification analysis (Figure 4E,F), but not CD31$^+$EMCN$^-$ or CD31$^-$EMCN$^+$ vessels (Figure S4B,C, Supporting Information). Also, the number of PCNA$^+$ proliferative cells around CD31$^+$EMCN$^+$ vessels was remarkably increased in the wound center area of CA group (Figure 4G,H), which indicated that CA-mediated enhancement of CD31$^+$EMCN$^+$ vessels provided a pro-regenerative microenvironment. Subsequently, to investigate whether the Notch signaling was involved, the expression level of NICD was detected in the wound center area, and results revealed that CA treatment significantly increased NICD expression, as determined by quantification of NICD$^+$CD31$^+$EMCN$^+$ vessels (Figure 4I,J). Similar results of cell proliferation and Notch signaling activation were observed in the wound edge area (Figure S5J–M, Supporting Information). Taken together, these data suggested that MSC-CAs provide an efficacious therapy for diabetic wound healing through inducing specialized vasculature with regeneration-relevant feature.

2.5. Suppression of Therapeutic Effects of CAs by Pharmacological Inhibition of EV Release

As to the underlying mechanism of CAs promoting CD31$^+$EMCN$^+$ vessels, in the following sections, we investigated whether the therapeutic effects were mediated by EVs, membranous nanovesicles revealed to play a key role in mediating stem cell therapy.[49,50] First, we used GW4869, a widely used EV biogenesis inhibitor,[51] to pretreat CAs and explored whether inhibiting EV secretion suppressed the therapeutic efficacy of CAs. As described above, CAs pretreated with GW4869 were applied to the wound area of db/db mice on the operation day with CAs as the control, and the wound area was photographed at various time points (**Figure 5**A). The quantification of residual wound area showed that, compared to the CA group, the wound closure rate in the CA+GW4869 group was significantly delayed throughout the whole healing period (Figure 5B). Histological analysis of the dissected skin tissues via H&E and Masson staining further showed that the therapeutic effects of CAs were remarkably diminished by GW4869 pretreatment (Figure S6A–E, Supporting Information). More importantly, after 10 d of treatment, the immunofluorescence co-staining of CD31 and EMCN demonstrated that GW4869 pretreatment significantly suppressed the promotive effects of CAs on CD31$^+$EMCN$^+$ vessel regrowth in both the wound center and edge areas, as confirmed by quantification analysis (Figure 5C–F), but not CD31$^+$EMCN$^-$ or CD31$^-$EMCN$^+$ vessels (Figure S4D,E, Supporting Information). Also, the increase of PCNA$^+$ proliferative

cells around CD31$^+$EMCN$^+$ vessels by CAs was remarkably repressed in the wound center area of CA+GW4869 group (Figure 5G,H). Moreover, detection of NICD expression in the wound center area showed that GW4869 pretreatment inhibited CA-induced activation of Notch signaling in CD31$^+$EMCN$^+$ vessels (Figure 5I,J). Similar results were observed in the wound edge area (Figure S6F–I, Supporting Information). These findings suggested that CA-EVs are involved to play an important role in CA-induced angiogenesis of CD31$^+$EMCN$^+$ vessels and enhancement of diabetic wound healing.

2.6. Enhancement of CD31$^+$EMCN$^+$ Vessel Regrowth and Alleviation of Diabetic Wound Healing by CA-Derived EVs

Next, we isolated and characterized CA-derived EVs according to our published protocol.[52] Intriguingly, compared with single MSCs in culture, MSC-CAs produced significantly more amount of EVs, as quantified by both calculating the protein ratio of EV to cell and the particle number (**Figure 6**A,B). Transmission electron microscope (TEM) observation showed that CA-EVs exhibited a typical sphere-like morphology with bilayer membrane structure (Figure 6C). Nanoparticle tracking analysis (NTA) measurement showed that the diameters of CA-EVs ranged from 50 to 500 nm and peaked at 150–250 nm (Figure 6D). Moreover, western blot analysis revealed the enrichment of EV markers, flotillin-1, caveolin-1, and CD9, as well as low expression of nuclear protein histone-3 (Figure 6E). Subsequently, we prepared proteins of CA-EVs and parental CAs, and performed liquid chromatography with tandem mass spectrometry (LC-MS/MS) analysis to evaluate the potential angiogenesis-related protein cargos of CA-EVs. A total of 5609 proteins were identified, within which 1167 were significantly upregulated in CA-EVs (Figure 6F). Notably, Gene Ontology (GO) enrichment analysis of the significantly upregulated proteins showed that multiple angiogenesis-related terms, including "sprouting angiogenesis," "angiogenesis," "regulation of sprouting angiogenesis," "regulation of angiogenesis," and "positive regulation of angiogenesis," were enriched in CA-EVs (Figure 6G). In line with the functional analysis, a variety of individual proteins participating in angiogenesis process were upregulated in the CA-EVs (Figure 6H). In addition, we have found three significantly upregulated proteins that were highly correlated with the Notch signaling pathway in CA-EVs, namely, nicastrin (NCSTN), presenilin-1 (PSEN1), and notch2 (NOTCH2) (Figure 6H). Collectively, these data indicated that aggregate culture increases the production of EVs that are enriched with a set of pro-angiogenic functional proteins.

Based on the above results, we subsequently investigated the protective effects of CA-EVs on ECs in vitro. First, PKH26-labeled EVs were added to cultured ECs and internalization of EVs was verified by confocal microscopy observation (Figure S7A, Sup-

---

(green) and EMCN (red) co-immunostaining in the wounded skin of PBS and CA groups at D10 post-treatment, counterstained by DAPI (blue). Scale bars, 100 µm. E,F) Quantification of fold changes of CD31$^+$EMCN$^+$ vessel area (% total area) at the wound center and edge area of PBS and CA groups at D10 post-treatment. G) CD31 (green), EMCN (red), and PCNA (white) co-immunostaining at the wound center area of PBS and CA groups at D10 post-treatment, counterstained by DAPI (blue). Scale bar, 100 µm. H) Quantification of fold change of PCNA$^+$ cells adjacent to CD31$^+$EMCN$^+$ vessels (% total area) at the wound center area of PBS and CA groups at D10 post-treatment. I) CD31 (green), EMCN (red), and NICD (white) co-immunostaining at the wound center area of PBS and CA groups at D10 post-treatment, counterstained by DAPI (blue). Scale bar, 100 µm. J) Quantification of fold change of NICD$^+$CD31$^+$EMCN$^+$ vessels at the wound center area of PBS and CA groups at D10 post-treatment. $n = 3$ per group. Data are presented as mean $\pm$ SD. **$P < 0.01$; ***$P < 0.001$; ****$P < 0.0001$.
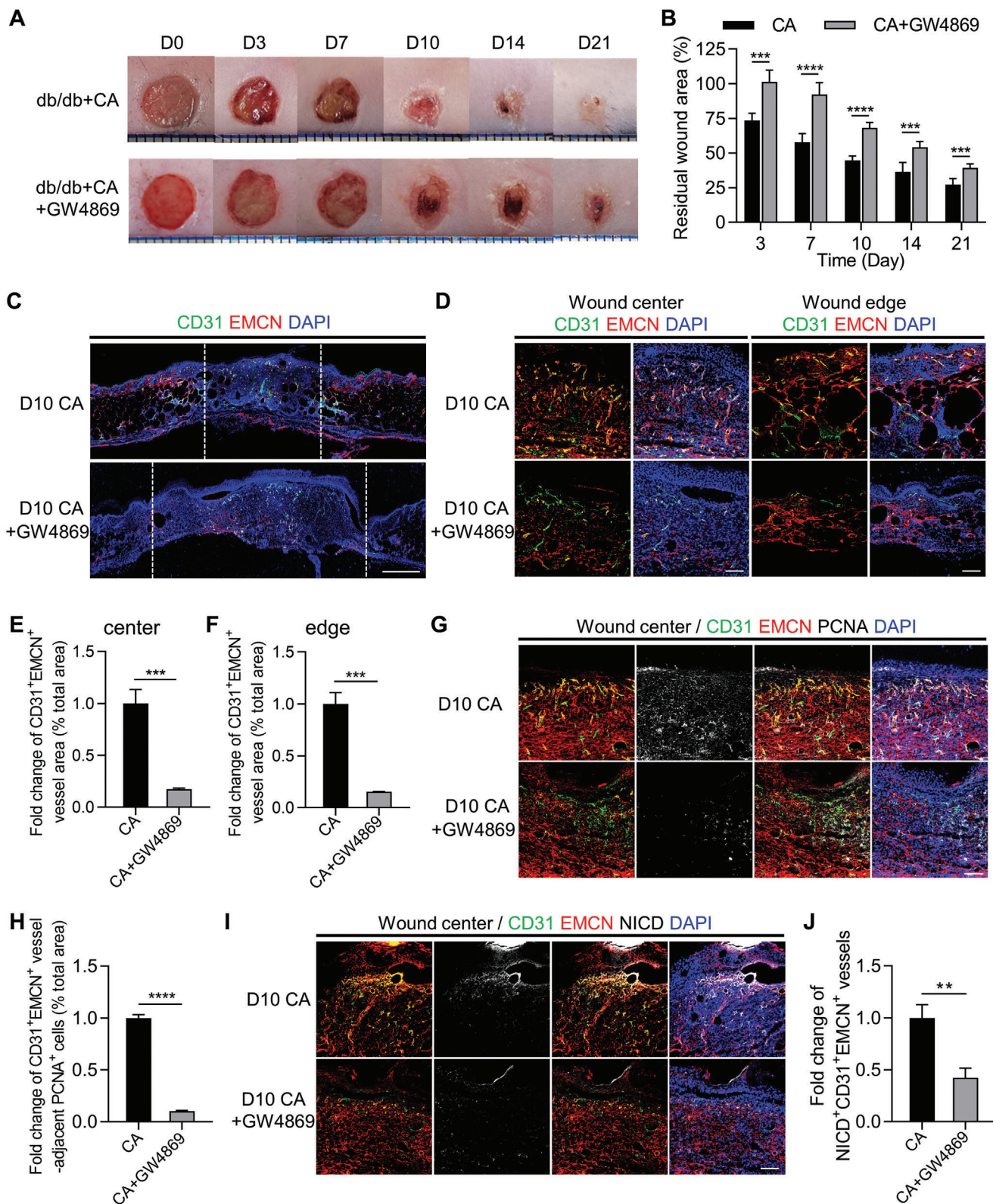
Figure 5. Suppression of skin regenerative effects of CAs by pharmacological inhibition of extracellular vesicle (EV) release. AB) Representative photographs of full-thickness cutaneous wounds in CA (control) and CA+GW4869 groups, and B) quantification of the residual wound area in each group. $n = 6$ per group. C) The low-magnified images of CD31 (green) and EMCN (red) co-immunostaining in the wounded skin of CA and CA+GW4869 groups at D10 post-treatment, counterstained by DAPI (blue). Scale bar, 1 mm. D) The high-magnified images of CD31 (green) and EMCN (red) co-

ADVANCED
SCIENCE NEWS

www.advancedsciencenews.com

ADVANCED
HEALTHCARE
MATERIALS

www.advhealthmat.de

porting Information). Then, high glucose and AGE treatments were performed as stated above, and CA-EVs were added to the culture system, with addition of PBS as the control. Scratch assay and tube formation assay showed that CA-EVs significantly rescued high glucose- or AGEs-induced impairment of the migration and tube formation ability of ECs (**Figure 7**A–D). Further quantification confirmed the above observation (Figure 7E–H). As for the formation of CD31+EMCN+ vessels in vitro, immunofluorescence staining showed that the inhibition of CD31+EMCN+ vessel formation by high glucose or AGE treatments was rescued by CA-EVs (Figure 7I–L). Moreover, the addition of CA-EVs remarkably increased the expression of NICD protein expression (Figure 7M–O), suggesting improvement of Notch signaling activity. Given the encouraging in vitro results, we further applied CA-EVs to the wound area of db/db mice on the operation day with PBS as the blank control, and evaluated their therapeutic effects in vivo (**Figure 8**A). Compared to the PBS group, CA-EV treatment significantly accelerated the wound closure rate (Figure 8B). Histological analysis of the dissected skin tissues via H&E and Masson staining further showed that CA-EV treatment remarkably enhanced skin healing (Figure S7B–F, Supporting Information), as shown by reduced defect area and well-organized regenerated skin structure. Of note, after 10 d of treatment, the immunofluorescence co-staining of CD31 and EMCN showed that CA-EVs significantly increased CD31+EMCN+ vessels in both the wound center and edge areas (Figure 8C,D), as confirmed by quantification analysis (Figure 8E,F), but not consistently CD31+EMCN− or CD31−EMCN+ vessels (Figure S4F,G, Supporting Information). Also, the number of PCNA+ proliferative cells around CD31+EMCN+ vessels was remarkably increased in both the wound center and edge areas of the CA-EV group (Figure 8G,H, and Figure S7G,H, Supporting Information), which suggested that enhancement of CD31+EMCN+ vessels by CA-EVs contributed to the establishment of a pro-regenerative microenvironment. Moreover, we detected the expression level of NICD in both the wound center and edge areas. Results showed that CA-EVs treatment significantly increased NICD expression, as determined by quantification of NICD+CD31+EMCN+ vessels (Figure 8I,J, and Figure S7I,J, Supporting Information). These data collectively suggested that CA-EVs are able to induce specialized vasculature in skin regeneration and improve diabetic wound healing.

3. Discussion

As a system essential for providing oxygen and nutrients to the tissue, the establishment and maintenance of vascular network is crucial for embryonic development, as well as subsequent postnatal life.[5,53] In the aspect of skin, the vessels are mainly distributed in the dermis, maintaining both dermal and epidermis

homeostasis.[18] Notably, when the skin is confronted with injury, the formation of new blood vessels from preexisting ones, a process named angiogenesis, takes place and represents an essential component for optimal wound healing.[2,3] Within recent years, it has been gradually elucidated that ECs which are lining the inner surface of the vasculature display a remarkable heterogeneity and plasticity.[5,6] Accordingly, the identification of distinct vessel subtypes has revolutionized our understanding of vascular biology. In this study, we add to the current knowledge on skin vasculature by identifying a specific vessel subtype that are featured by simultaneous CD31 and EMCN expression and functionally participate in the regeneration process under both physiological and pathological conditions, as well as respond to therapeutic intervention. These findings will be beneficial for future studies in skin basic and medical research.

The combination of CD31 and EMCN that we used in our research to characterize a specific vessel subtype was first reported in bone, where the vasculature was named type H vessels.[54,55] These vessels are mainly located near the growth plate in the metaphysis, constituting a metabolically specialized microenvironment rich in oxygen and nutrients, and with close proximity of osteoprogenitors.[7,48,56] Collectively, type H vessels play pivotal roles in mediating growth of blood vessels and coupling of osteogenesis and angiogenesis.[7,48,56] Moreover, in bone diseases such as aging and postmenopausal osteoporosis, the number of type H vessels was remarkably decreased, which was also found in aged and osteoporotic individuals, indicating that type H vessels are indeed present in human bones.[57,58] In this field, we have previously identified a specific MSC subset marked by Gli1 to couple with type H vessels in bone, and discovered that Gli1+MSCs drive CD31+EMCN+ vessels to initiate bone fracture healing.[59] Intriguingly, our current study further extends the understanding of this field by demonstrating the presence of CD31+EMCN+ vessels in skin, which prompts us to assume that the existence of vessel subtypes with the same markers as type H vessels may be a common phenotype across a variety of organs. Also, it should be noted that given the tissue specificity, the skin CD31+EMCN+ vessels possess distinct functional features than those in the bone, such as being coupled with proliferative but not osteogenic cells, although they may actually represent a common function to promote tissue formation. Future studies will be required to reveal the nature of these vessels by digging into their molecular profiles in diverse organ niches. Further works are also in demand with spatial transcriptomics and transgenic technique to uncover the specific modulation factors for skin CD31+EMCN+ vessels, their difference with other vessel subtypes, and their interaction with neighboring cells.

The diabetes, especially T2D that has become a major global health epidemic, is a leading cause for nonhealing wounds.[60,61] For now, common strategies for managing diabetic wounds

immunostaining in the wounded skin of CA and CA+GW4869 groups at D10 post-treatment, counterstained by DAPI (blue). Scale bars, 100 μm. E,F) Quantification of fold changes of CD31+EMCN+ vessel area (% total area) at the wound center and edge area of CA and CA+GW4869 groups at D10 post-treatment. G) CD31 (green), EMCN (red), and PCNA (white) co-immunostaining at the wound center area of CA and CA+GW4869 groups at D10 post-treatment, counterstained by DAPI (blue). Scale bar, 100 μm. H) Quantification of fold change of PCNA+ cells adjacent to CD31+EMCN+ vessels (% total area) at the wound center area of CA and CA+GW4869 groups at D10 post-treatment. I) CD31 (green), EMCN (red), and NICD (white) co-immunostaining at the wound center area of CA and CA+GW4869 groups at D10 post-treatment, counterstained by DAPI (blue). Scale bar, 100 μm. J) Quantification of fold change of NICD+CD31+EMCN+ vessels at the wound center area of CA and CA+GW4869 groups at D10 post-treatment. n = 3 per group. Data are presented as mean ± SD. **P < 0.01; ***P < 0.001; ****P < 0.0001.
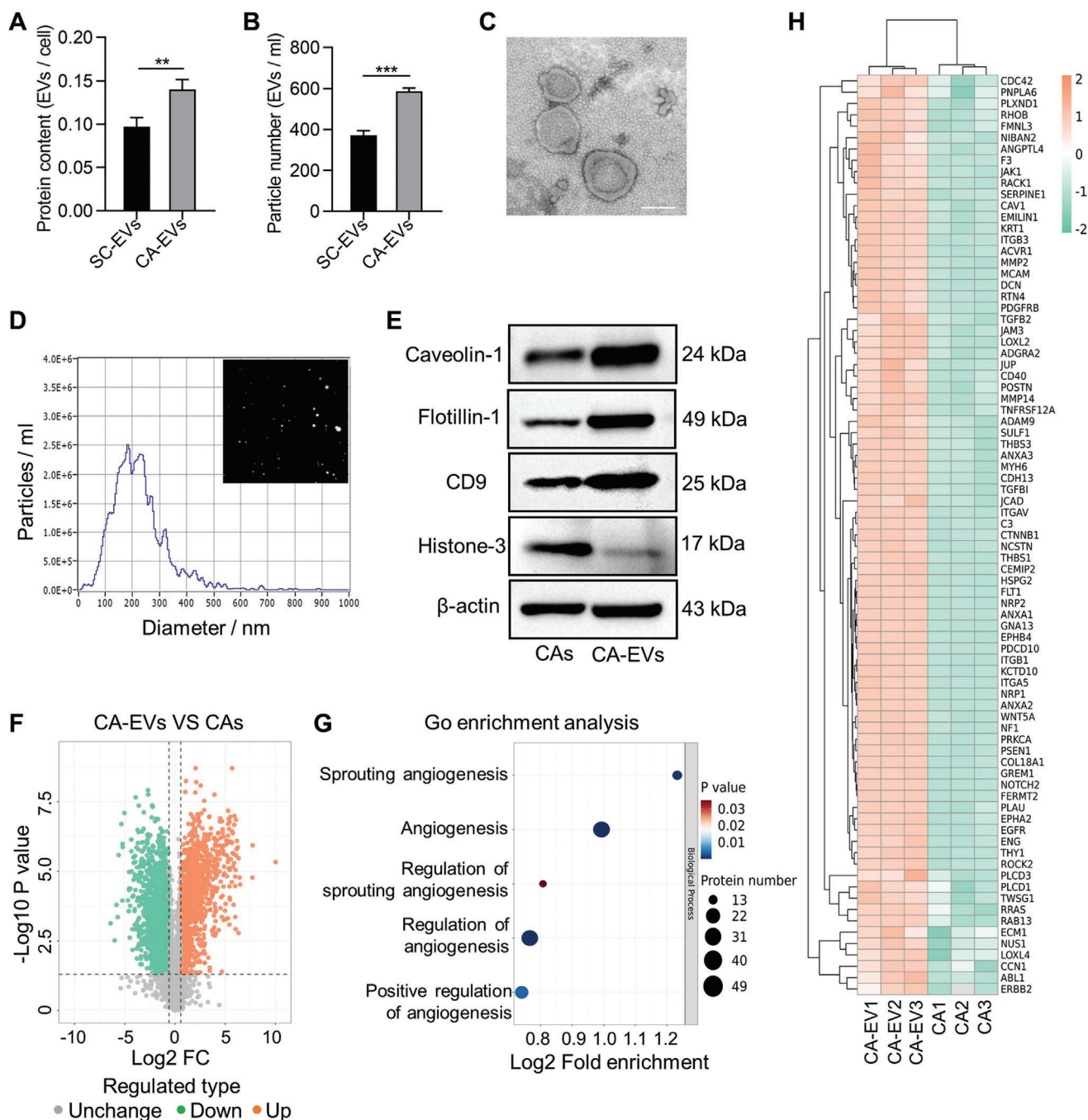
Figure 6. Characterization and proteomic analysis of CA-derived EVs. A) Quantification of protein content of single cell-derived EVs (SC-EVs) and CA-EVs. B) Quantification of particle number of SC-EVs and CA-EVs. C) Representative transmission electron microscope (TEM) image of CA-EVs. Scale bar, 200 nm. D) Representative nanoparticle tracking analysis (NTA) image of CA-EVs. E) Western blotting analysis showing the protein markers of CAs and CA-EVs. F) Volcano plot showing significantly upregulated (orange dots) and downregulated (green dots) proteins in CA-EVs, compared to CAs. G) Gene ontology (GO) enrichment analysis of significantly upregulated proteins in CA-EVs. The Y-axis represents angiogenesis-related GO terms and the X-axis represents fold enrichment. The color of the bubble represents enrichment significance and the size of the bubble represents number of upregulated proteins. H) Hierarchical clustering of the proteins involved in the GO terms in (G), with protein abundance being Z-score normalized. Rows represent proteins and columns represent individual replicates. $n = 3$ per group. $**P < 0.01$; $***P < 0.001$.
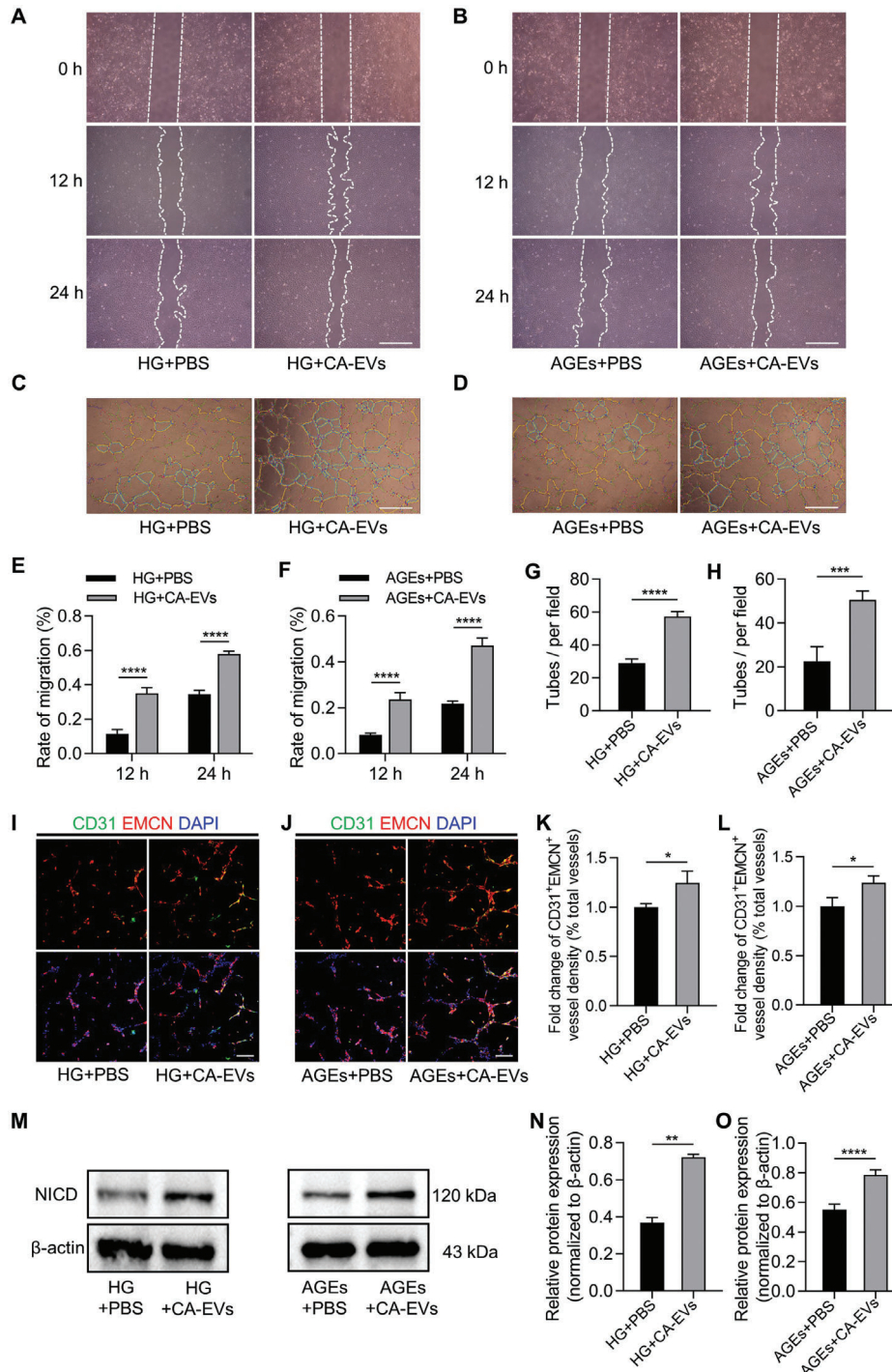
Figure 7. Enhancement of CD31$^+$EMCN$^+$ vessel formation by CA-EVs. A) Representative images of scratch assay of HUVECs treated by high glucose (HG), with addition of PBS or CA-EVs at indicated timepoints. Scale bar, 500 μm. B) Representative images of scratch assay of HUVECs treated by advanced glycation end products (AGEs), with addition of PBS or CA-EVs at indicated timepoints. Scale bar, 500 μm. C) Representative images of tube formation assay of HUVECs treated by HG, with addition of PBS or CA-EVs. Scale bar, 500 μm. D) Representative images of tube formation assay of HUVECs treated by AGEs, with addition of PBS or CA-EVs. Scale bar, 500 μm. E) Quantification of migration rate of HUVECs in (A). F) Quantification of migration rate of HUVECs in (B). $n = 5$ per group. G) Quantification of formed tubes of HUVECs in (C), as indicated by blue circles. H) Quantification of formed tubes of HUVECs in (D), as indicated by blue circles. $n = 4$ per group. I) CD31 (green) and EMCN (red) co-immunostaining of HUVECs in (C), counterstained by DAPI (blue). Scale bar, 100 μm. J) CD31 (green) and EMCN (red) co-immunostaining of HUVECs in (D), counterstained by DAPI (blue). Scale bar, 100 μm. K) Quantification of CD31$^+$EMCN$^+$ vessel density (% total vessels) in (I). L) Quantification of CD31$^+$EMCN$^+$ vessel density (% total vessels) in (J). M) Western blotting analysis of NICD protein in HUVECs. N,O) Quantification of the protein expression level of NICD, normalized to β-actin. $n = 3$ per group. Data are presented as mean ± SD. *$P < 0.05$; **$P < 0.01$; ***$P < 0.001$; ****$P < 0.0001$.
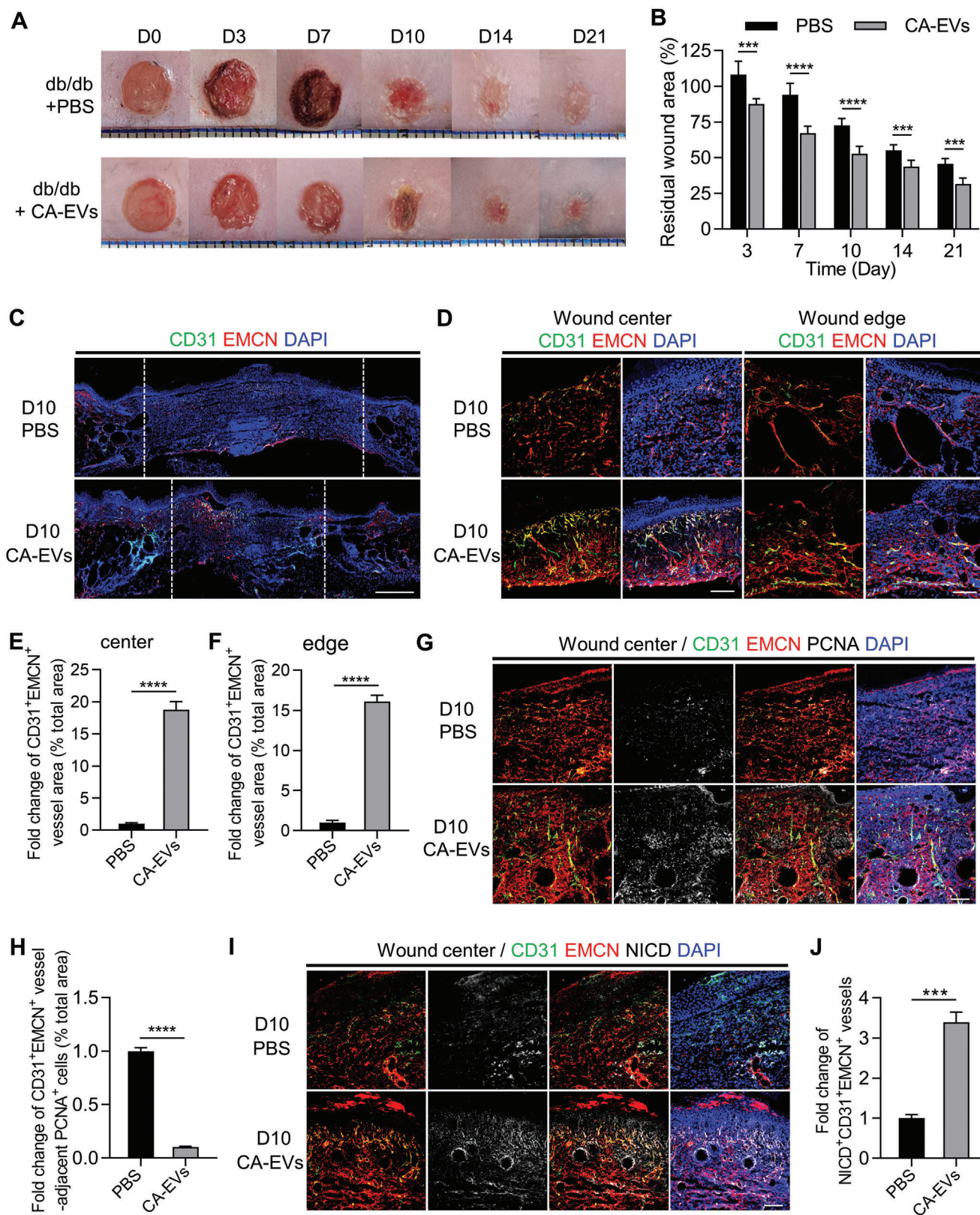
Figure 8. Enhancement of CD31$^+$EMCN$^+$ vessel regrowth and alleviation of diabetic wound healing by CA-EVs. A) Representative photographs of full-thickness cutaneous wounds in PBS (control) and CA-EVs groups, and B) quantification of the residual wound area in each group. $n = 6$ per group. C) The low magnification images of CD31 (green) and EMCN (red) co-immunostaining in the wounded skin of PBS and CA-EVs groups at D10 post-

mainly include debridement, dressings, negative pressure and hyperbaric oxygen therapy.[16,17] Nevertheless, the currently available treatments are only moderately effective, thus the development of better therapies is in great need. Notably, the impaired ability to regrow microvasculature through angiogenesis is a major aspect in the nonhealing nature of diabetic wounds, putatively attributed to general mechanisms involving oxidative stress.[19,21,62] Here, we provide a new perspective that decline of regeneration-relevant $CD31^+EMCN^+$ vessels and the concomitant reduction of proliferative cells potentially offer a compelling explanation to diabetic wounds. As to the underlying molecular mechanism, we have focused on Notch signaling that text-dependently play controversial roles in angiogenesis.[63] Particularly, previous studies have reported that Notch signaling is positively related with the proliferation and angiogenesis of type H vascular ECs.[48,64] We further reveal that Notch signaling was inhibited in skin $CD31^+EMCN^+$ vessels under T2D condition. Our results will be of great importance to provide target for future studies on nonhealing conditions involving T2D.

Stem cell-based therapies arise to exhibit enormous potential for promoting the regeneration of nonhealing wounds in both preclinical studies and clinical trials.[65–67] Of note, the key focus is on MSCs that can be easily isolated from various tissue sources and exert therapeutic activity by homing to injury sites and modulating the recipient environment.[68–70] However, the efficacy of MSCs is compromised by the common injection strategy, due to limited cell survival, retention and engraftment.[71,72] Therefore, we have developed MSC-derived CAs for regenerative application, which hold the great amount of cell-deposited natural ECM with intact cell–cell and cell–ECM interactions to promote survival, functionality, and communication of cells within.[38–41] Intriguingly, the concept of CAs is a paradigm for recapitulating the developmental mesenchymal condensation process through tissue engineering efforts. Our own works, as well as other's studies, have verified that the implanted MSC-based CAs continue to differentiate in recipients and induce vascularization and innervation likely through paracrine mechanisms.[33,38,39] Here, we further demonstrate that MSC-CAs are useful for improving diabetic wound healing and enhancing angiogenesis of regeneration-relevant $CD31^+EMCN^+$ vessels, with upregulation of Notch signaling. It is noteworthy that the embryonic dermal condensate is the precursor to the permanent mesenchymal unit of the hair follicle responsible for postnatal hair cycling,[33] yet whether the developmental condensation phenomenon coordinates vascularization in skin remains to be further elucidated.

EVs are lipid bilayered particles secreted from almost all the cell types in the body and loaded with various signaling biomolecules, including proteins, lipids and nucleic acids.[73] Although initially considered as cellular wastes, EVs have now been recognized as important constituents in intercellular communication with physiological and pathological functions.[74] Notably, recent studies of the MSC therapeutic mechanism have revealed that the positive effects of MSCs are importantly mediated via EVs.[49,75–77] In this study, we have verified the involvement of EVs through pharmaceutical inhibition of EV release from CAs. We have further elucidated that the aggregating culture increased EV production, and that CA-EVs themselves exert encouraging effects to stimulate regeneration-relevant $CD31^+EMCN^+$ vessels and improve diabetic wound healing. In addition, proteomics analysis has showed difference between EVs and their parental CAs regarding the angiogenic protein cargos, suggesting that in addition to inheriting the functional properties of the parental cells, EVs may exhibit more prominent angiogenic functions. The mechanisms of aggregation promoting EV release remain to be further elucidated. Of the EV carrying proteins, nicastrin and presenilin-1 are important components of the γ-secretase complex, suggesting that CA-EVs may activate the Notch signaling pathway of ECs to promote its angiogenesis by transporting γ-secretase-related proteins. However, whether the mature γ-secretase is active in EVs and EVs work through γ-secretase is unclear, which will also be explored in the future. Importantly, the application of EVs as therapeutic reagents possesses many advantages, including easy storage for a longer duration, higher penetration efficiency for skin, less risk of immune response activation, and being easy to be engineeringly modified.[49,75] Notably, the mechanism of CA effect is not limited to CA-EVs. Our experiments also found that there was still a light efficacy after inhibiting the secretion of EVs from CAs, which may be attributed to the large number of ECM deposited and other secreted growth factors and cytokines of CAs. For example, as reported, ECM in the injured tissue was commonly lost, thus lacking matrix for supporting constructive communication between endogenous cells would prevent the tissue repair.[78] Accordingly, ECM has been reported to be beneficial to the repair of skin defects,[78,79] and our established CAs are well-known to enrich for ECM, including collagens, fibronectin, laminin, proteoglycans, and glycoproteins.[40,42] Despite these potential contributions, CA-EVs indeed promoted wound healing in this study, indicating that CA-EVs do play a very important role in mediating the CA effect. Thus, our findings will help to establish optimized feasible strategies to counteract diabetic wounds based on CA-EVs.

Collectively, these results extend the current understanding of skin vasculature by identifying a specialized regeneration-relevant vessel subtype that play important roles in normal and diabetic wound healing, as well as in stem cell-based regenerative therapy, which provides a potent rational for translational paradigms.

---

treatment, counterstained by DAPI (blue). Scale bar, 1 mm. D) The high-magnification images of CD31 (green) and EMCN (red) co-immunostaining in the wounded skin of PBS and CA-EVs groups at D10 post-treatment, counterstained by DAPI (blue). Scale bars, 100 µm. E,F) Quantification of fold changes of $CD31^+EMCN^+$ vessel area (% total area) at the wound center and edge area of PBS and CA-EVs groups at D10 post-treatment. G) CD31 (green), EMCN (red), and PCNA (white) co-immunostaining at the wound center area of PBS and CA-EVs groups at D10 post-treatment, counterstained by DAPI (blue). Scale bar, 100 µm. H) Quantification of fold change of $PCNA^+$ cells adjacent to $CD31^+EMCN^+$ vessels (% total area) at the wound center area of PBS and CA-EVs groups at D10 post-treatment. I) CD31 (green), EMCN (red) and NICD (white) co-immunostaining at the wound center area of PBS and CA-EVs groups at D10 post-treatment, counterstained by DAPI (blue). Scale bar, 100 µm. J) Quantification of fold change of $NICD^+CD31^+EMCN^+$ vessels at the wound center area of PBS and CA-EVs groups at D10 post-treatment. $n = 3$ per group. Data are presented as mean $\pm$ SD. $^{***}P < 0.001$; $^{****}P < 0.0001$.

4. Experimental Section

Animals: Animal experiments were performed in accordance with the Guidelines of Intramural Animal Use and Care Committees of The Fourth Military Medical University and the ARRIVE guidelines. One-week and 10-week-old male C57BL/6 mice were purchased from the Laboratory Animal Center of the Fourth Military Medical University, as we have used in previous studies.[80] Ten-week-old male diabetic db/db (BKS.Cg-Dock7^m +/+Lepr^{db}/J) mice and nondiabetic control db/m mice with the same background were purchased from Cavens Lab Animal Co., Ltd. (Changzhou, China). All mice were maintained under specific pathogen-free conditions (24 °C, 12 h light/dark cycles and 50% humidity), and fed with food and water at libitum.

Cell Culture: The human umbilical cord-derived MSC (UCMSC) line was purchased from the American Type Culture Collection (ATCC) and cultured with alpha-minimum essential medium (α-MEM, Invitrogen, USA) supplemented with 10% fetal bovine serum (FBS, Sijiqing, China), 2 × 10^{-3} M L-glutamine (Invitrogen, USA) and 1% penicillin/streptomycin (Invitrogen, USA) in a humidified atmosphere of 5% CO_2 at 37 °C. The medium was refreshed every 2 d, and the cells were passaged once they were 80%–90% confluent. For CA culture, UCMSCs were seeded into six-well plates at 3 × 10^5 cells/well or 10-cm culture dishes at 1 × 10^6 cells/dish with the above medium. When the cells reached 80% confluence, the medium was changed to α-MEM containing 50 μg mL^{-1} vitamin C (MP Biomedicals, USA), 10% FBS, 2 × 10^{-3} M L-glutamine, and 1% penicillin/streptomycin, which was refreshed every 2 d. After about 7 d, CA with white membrane-like structures was formed and detached from the culture plates with a cell scraper. The HUVECs were purchased from the ATCC and cultured in endothelial cell medium (ECM) (Sciencell, USA), according to the instructions. The medium was refreshed every 3 d, and the cells were passaged once they were 80%–90% confluent.

Characterization of CAs: Mature CAs were fixed with 4% paraformaldehyde (PFA) overnight and harvested with a cell scraper. After dehydration through graded ethanol, the samples were embedded in paraffin and sectioned slices underwent H&E staining. As for SEM observation, mature CAs were fixed with glutaraldehyde overnight, dehydrated and dried with hexamethyldisilane. The dried samples were stuck onto the sample table with double-sided carbon tape and coated with gold. Further observation was performed with a SEM (Hitachi S-4300, EIKO Engineering, Japan).

Collection of EVs: EVs were collected as described before.[52] Briefly, 5 d after the induction of CA in 10-cm dishes, the medium was substituted with fresh inducing medium containing EV-depleted FBS obtained by ultracentrifugation at 100 000 *g* for 18 h. After 48 h, the supernatant was collected and centrifuged at 800 *g* for 10 min to remove cells and debris. The supernatant was further collected and centrifuged at 16 000 *g* for 30 min to obtain EVs, followed by washing twice with PBS. EV preparations were characterized by NTA, TEM, and mass spectrometry EVs were quantified by measuring the total protein concentration via a BCA Protein Assay Kit (TIANGEN, China). The size and morphology of EVs were assessed using a TEM (Thermo fisher, USA). The size distribution of EVs was quantitated using NTA with a PMX Zetaview (Particle Metrix, Germany). The expression of marker proteins in EVs was examined by western blot analysis.

Proteomic Analysis: Protein lysates of UCMSC-CAs and EVs secreted by UCMSC-CAs were prepared and subjected to LC-MS/MS analysis on an Orbitrap Exploris 480 mass spectrometer with a NanoSpray III ion source. The raw data were analyzed using Proteome Discoverer software (v2.4.1.15). Proteins were identified by comparing against the Uniport database with a false discovery rate set at 0.01 for both peptides and proteins. Proteins were quantified using the default parameters in MaxQuant. Among the identified proteins, differentially expressed proteins (DEPs) (fold change > 1.5 and *P*-value < 0.05) were included for further functional analysis based on GO database. Protein–protein interaction (PPI) analysis was performed on the STRING online database (http://string-db.org), and the network was constructed and visualized using Cytoscape 3.8.0 software.

Establishment of Skin Wound Healing Model: Cutaneous wounds were created as previously described.[81] The mice were anesthetized by intraperitoneal injection of pentobarbitone sodium. After shaving and clean-ing, two 6-mm full-thickness wounds were made on the dorsal skin on each side of the midline using a sterile punch biopsy tool (HEAD, China) and a scissor. The digital photographs of the wounds were taken every 3–4 d and analyzed by the ImageJ software (NIH, USA). The wound healing rate was calculated according to the following equation: Residual wound area (%) = Actual wound area/Original wound area × 100%. Immunofluorescent analyses were performed at day 3, 7, and 14, and histological analyses were performed at day 14.

To explore the therapeutic effects of CAs, the wounded db/db mice were allocated to two groups: the CA group in which the UCMSC-CA of one sheet was harvested and tiled on the wound area with 25 μL PBS, and the PBS group was performed by the dropwise addition of 25 μL PBS to the defect area after skin defect to mimic the procedure of CA addition. To explore the role of EV secretion in the therapeutic effects of CAs, the wounded db/db mice were allocated to two groups: the CA group as described above and the CA-GW4869 group in which the applied CAs were pretreated with the EV release inhibitor, GW4869 (MCE, China) at 10 × 10^{-6} M for 24 h. To further explore the therapeutic effects of CA-EVs, the wounded db/db mice were allocated to two groups: the CA-EVs group in which ≈30 μg EVs (on the basis of protein measurement) suspended in 100 μL PBS were injected into the subcutaneous layer at four points around the wound bed (≈2–3 mm from the wound edge), and the PBS group was performed by equal volume of PBS injection in the same way to mimic the procedure of EV addition. The wounds were initially covered by surgical dressings (3M, USA), which was removed after 48 h and the wound areas were digitally measured and quantified as stated above. Immunofluorescent analyses were performed at day 10 and histological analyses were performed at day 21.

Immunofluorescent Staining: Fresh skin tissue samples were fixed in 4% PFA (Biosharp, China) at 4 °C for 4 h, washed twice with PBS and dehydrated with 30% sucrose for 16–18 h. After being embedded in optimal cutting temperature (OCT) compound (Leica, Germany), 20 μm cryosections were produced with a cryastat (CM1950, Leica, Germany) and underwent immunofluorescent staining, as previously reported.[82] Briefly, air-dried cryosections were permeabilized by 0.3% Triton X-100 (Sigma-Aldrich, USA) for 20 min at room temperature, blocked in goat serum (BOSTER, China) for 30 min at room temperature and incubated with the primary antibodies overnight at 4 °C. The following primary antibodies were used: anti-CD31 (FAB3628G, R&D Systems, USA; diluted 1:100) which is conjugated with Alexa Fluor 488, anti-EMCN (sc-65495, Santa Cruz Biotechnology, USA; diluted 1:100), anti-PCNA (13110T, Cell Signaling Technology, USA; diluted 1:100), and anti-NICD (3608S, Cell Signaling Technology, USA; diluted 1:100). Then, the cryosections were washed with PBS for three times and incubated with the fluorescence-conjugated secondary antibodies at room temperature for 1 h. The following secondary antibodies were used: Cy3-conjugated goat anti-rat IgG (33308ES60, YEASEN, China; diluted 1:200) and Alexa Fluor 647-conjugated donkey anti-rabbit IgG (ab150075, Abcam, UK; diluted 1:200). Subsequently, after washing with PBS for three times, the slides were mounted with Mounting Medium With DAPI-Aqueous, Fluoroshield (Abcam, UK).

Images were acquired by a confocal laser scanning microscopy (CLSM) (Nikon A1+, Nikon, Japan) and analyzed using the ImageJ software (NIH, USA) and the Image-Pro Plus software (Media Cybernetics, USA) according to a previous report.[59] Z stacks of high-magnification images were scanned at high resolution and were processed and reconstructed in three dimensions with the NIS-Elements Viewer software (version 5.21, Nikon, Japan). Quantification of CD31$^+$EMCN$^+$, CD31$^-$EMCN$^+$, CD31$^+$EMCN$^-$, and NICD$^+$CD31$^+$EMCN$^+$ vessels was carried out with ImageJ software (Figure S1A, Supporting Information). Briefly, red area means CD31$^-$EMCN$^+$ vessels, green area means CD31$^+$EMCN$^-$ vessels, yellow area means CD31$^+$EMCN$^+$ vessels, and white area means PCNA$^+$ or NICD$^+$ cells. The ImageJ was used to analyze the proportion of red, green, yellow, or white areas to the total visual area (% total area), and their respective areas to the total blood vessel area (% total vessels). Quantification of the PCNA$^+$ cells adjacent to CD31$^+$EMCN$^+$ vessels was carried out with the Image-Pro Plus software. Specifically, an area around the CD31$^+$EMCN$^+$ vessels with a range of 20 μm was lined out and the fluorescence signals (parameter: area sum) within this area were quantified,

ADVANCED
SCIENCE NEWS

www.advancedsciencenews.com

ADVANCED
HEALTHCARE
MATERIALS

www.advhealthmat.de

which was regarded as the PCNA$^+$ cells adjacent to CD31$^+$EMCN$^+$ vessels (Figure S1B, Supporting Information). When CD31$^+$EMCN$^+$ vessels and NICD were co-stained, the yellow and white overlapping area to the total field area was regarded as the proportion of NICD$^+$CD31$^+$EMCN$^+$ vessels. For some indexes, after absolute quantification of the signals, relative quantification was performed by taking the numerical value of one group as the reference and calculating the relative values of other groups, shown as the fold changes.

Histological Staining: Fresh skin tissue samples were fixed in 4% PFA for 10–12 h and underwent dehydration through graded ethanol. Then, the samples were embedded in paraffin and sectioned at 3 μm per slice. H&E staining and Masson staining were performed with commercial staining kits (Baso Technology, China), as previously described,[83] and images were taken using the SLIDEVIEW VS200 (Olympus, Japan).

EV Uptake Assay: To detect the uptake of EVs by HUVECs in vitro, HUVECs were seeded at 4000 cell/well in the ibidi angiogenesis μ-Slide (ibidi, Germany). After 24 h, EVs were labeled with PKH26 (Sigma-Aldrich, USA) according to previous experience[80] and added to cultured HUVECs at 10 μg mL^{-1}. Since the adding of the EVs, it is important to keep the cells from the light. After incubation for 24 h, HUVECs were washed with PBS and fixed in 4% PFA for 30 min at room temperature, followed by washing with PBS and blocking in goat serum for 30 min at room temperature. Then, HUVECs were incubated overnight at 4 °C with the following primary antibody: anti-CD31 (FAB3628G, R&D Systems, USA; diluted 1:100) which was conjugated with Alexa Fluor 488. After washing with PBS, HUVECs underwent nuclei counterstaining with DAPI (Sigma-Aldrich, USA) for 10 min at room temperature. Finally, after further washing with PBS, HUVECs were preserved in PBS at 4 °C. Fluorescence imaging was carried out by a CLSM (Nikon A1+, Nikon, Japan) and analyzed using the ImageJ software (NIH, USA).

Cell Migration Assay: The HUVECs were seeded into six-well plates at 5 × 10^5 cells/well and the scratch assay was performed to evaluate their migration ability, as previously reported. In brief, when the cells reached 90% confluence, sterile 200 μL pipette tips were used to create scratches on the plates by scraping cells away. After washing with PBS, the medium was changed into culture medium without FBS. For low glucose (LG) and high glucose (HG) treatment, 5 and 25 × 10^{-3} M glucose (Invitrogen, USA) was added into the media, respectively, and for mannitol (MA) treatment as the osmotic control, 20 × 10^{-3} M mannitol (Invitrogen, USA) was added together with 5 × 10^{-3} M glucose. For AGE treatment, 200 μg mL^{-1} AGE-bovine serum albumin (BSA) (Cayman Chemical, USA) dissolved in PBS was added to the medium, with equivalent PBS as the control. In addition, for the application of EVs, 10 μg mL^{-1} CA-EVs dissolved in PBS were added into specific wells as indicated. Scratches were photographed at 0, 12, and 24 h with an inverted microscope (Leica, Germany). Quantification of the scratch area was performed using the ImageJ software (NIH, USA).

Tube Formation Assay: The formation of capillary network was determined by in vitro tube formation assay on the ibidi angiogenesis μ-Slide (ibidi, Germany) precoated with Matrigel (Shanghai NovaMedical Technology, China). The HUVECs were seeded at 2 × 10^5 cells mL^{-1} (50 μL of medium for each well) and incubated in culture medium without FBS. The specific treatments were the same as described in the migration assay. Tube formation was photographed at 5 h with an inverted microscope (Leica, Germany). The number of network structures was quantified by measurement of five randomly selected microscopic fields using the ImageJ software (NIH, USA).

CD31$^+$EMCN$^+$ Vessel Formation Assay: The HUVECs were seeded at 4000 cells/well in the ibidi angiogenesis μ-Slide (ibidi, Germany) precoated by Matrigel (Shanghai NovaMedical Technology, China). After 5 h of treatment as described in the migration and tube formation assays, the cells were washed with PBS and fixed with 4% PFA for 30 min at room temperature, followed by washing with PBS and blocking in goat serum for 30 min at room temperature. Then, HUVECs were incubated overnight at 4 °C with the following primary antibodies: anti-CD31 (FAB3628G, R&D Systems, USA; diluted 1:100) which was conjugated with Alexa Fluor 488 and anti-EMCN (DF13357, Affinity, China; diluted 1:100). After washing with PBS, HUVECs were incubated with Cy3-conjugated goat anti-rat IgG antibody at room temperature for 1.5 h, followed by washing with PBS and

nuclei counterstaining with DAPI (Sigma-Aldrich, USA) for 10 min at room temperature. Finally, after washing with PBS, HUVECs were preserved in PBS at 4 °C. Fluorescence imaging was carried out by a CLSM (Nikon A1+, Nikon, Japan) and analyzed using the ImageJ software (NIH, USA).

Western Blot Analysis: Western blot was carried out as previously reported.[84] Briefly, cell and EV lysates were prepared using the Cell Lysis Buffer (Beyotime, China) containing protease inhibitor (Roche, Switzerland). After protein extraction and quantification using a BCA Protein Assay Kit (TIANGEN, China), 20 μg extracted proteins were separated by sodium dodecyl sulfate-polyacrylamide gels, transferred onto polyvinylidene fluoride membranes (Roche, Switzerland) and blocked in 5% BSA (MP Biomedicals, USA) for 2 h at room temperature. The membranes were incubated overnight at 4 °C with the following primary antibodies: anti-NICD (3608S, Cell Signaling Technology, USA; diluted 1:1000), β-actin (CW0096A, CWBio, China; diluted 1:1000), caveolin-1 (sc-53564, Cruz Biotechnology, USA; diluted 1:1000), flotillin-1 (18634, Cell Signaling Technology, USA; diluted 1:1000), CD9 (ET-1601-9, Huabio, China; diluted 1:1000), and histone-3 (9715, Cell Signaling Technology, USA; diluted 1:1000). Then, the membranes were washed three times with Tris-buffered saline-Tween (TBS-T, Solarbio, China) and incubated with peroxidase-conjugated secondary antibodies for 1 h at room temperature. After further washing with TBS-T, the protein bands were visualized with an enhanced chemiluminescence kit (4A Biotech, China) and evaluated with a gel imaging system (4600, Tanon, China).

Statistical Analysis: All the data were presented as mean ± standard deviation (SD). For two group comparisons, statistical significance was assessed by Student's *t*-test (two-tailed) while for multiple group comparisons, statistical significance was assessed by one-way ANOVA with Tukey's post hoc test. Values of $P < 0.05$ were considered statistically significant. Statistical and graph analyses were performed using GraphPad Prism 8.0 (GraphPad Software, USA).

Supporting Information

Supporting Information is available from the Wiley Online Library or from the author.

Acknowledgements

Conflict of Interest

The authors declare no conflict of interest.

Author Contributions

L.L. and C.-X.Z. contributed equally to this work. Conceptualization: F.J., Y.J., and B.-D.S.; Methodology: L.L., C.-X.Z., N.Z., T.Z., and C.-B.H.; Investigation: L.L., C.-X.Z., N.Z., J.C., and K.-C.Z.; Visualization: L.L., C.-X.Z., S.Z., J.-X.L., Z.K., and H.J.; Supervision: F.J., Y.J., and B.-D.S.; Writing—original draft: L.L. and C.-X.Z.; Writing—review & editing: F.J., Y.J., and B.-D.S.

Data Availability Statement

The data that support the findings of this study are available from the corresponding author upon reasonable request.

**ADVANCED
SCIENCE NEWS**

www.advancedsciencenews.com

**ADVANCED
HEALTHCARE
MATERIALS**

www.advhealthmat.de

Keywords

[1] F. M. Watt, *Science* **2014**, *346*, 937.
[2] M. Rodrigues, N. Kosaric, C. A. Bonham, G. C. Gurtner, *Physiol. Rev.* **2019**, *99*, 665.
[3] S. A. Eming, P. Martin, M. T. Canic, *Sci. Transl. Med.* **2014**, *6*, 265.
[4] G. C. Gurtner, S. Werner, Y. Barrandon, M. T. Longaker, *Nature* **2008**, *453*, 314.
[5] E. Trimm, K. Red-Horse, *Nat. Rev. Cardiol.* **2023**, *20*, 197.
[6] H. G. Augustin, G. Y. Koh, *Science* **2017**, *357*, aal2379.
[7] A. P. Kusumbe, S. K. Ramasamy, R. H. Adams, *Nature* **2014**, *507*, 323.
[8] G. Caligiuri, *Circ. Res.* **2020**, *126*, 1178.
[9] P. Lertkiatmongkol, D. Liao, H. Mei, Y. Hu, P. J. Newman, *Curr. Opin. Hematol.* **2016**, *23*, 253.
[10] S. M. Morgan, U. Samulowitz, L. Darley, D. L. Simmons, D. Vestweber, *Blood* **1999**, *93*, 165.
[11] G. Zhang, X. Yang, R. Gao, *Anim. Models Exp. Med.* **2021**, *3*, 325.
[12] D. B. Gurevich, D. T. David, A. Sundararaman, J. Patel, *Cells* **2021**, *10*, 2338.
[13] Q. Li, Z. Zhu, L. Wang, Y. Lin, H. Fang, J. Lei, T. Cao, G. Wang, E. Dang, *Theranostics* **2021**, *11*, 6461.
[14] Y. He, C. Tacconi, L. C. Dieterich, J. Kim, G. Restivo, E. Gousopoulos, N. Lindenblatt, M. P. Levesque, M. Claassen, M. Detmar, *Cells* **2022**, *11*, 1111.
[15] F. Berthiaume, H. C. Hsia, *Annu. Rev. Biomed. Eng.* **2022**, *24*, 61.
[16] H. Brem, M. Tomic-Canic, *J. Clin. Invest.* **2007**, *117*, 1219.
[17] S. Matoori, A. Veves, D. J. Mooney, *Sci. Transl. Med.* **2021**, *13*, abe4839.
[18] U. A. Okonkwo, L. A. DiPietro, *Int. J. Mol. Sci.* **2017**, *18*, 1419.
[19] W. B. Horton, E. J. Barrett, *Endocr. Rev.* **2021**, *42*, 29.
[20] J. Zhao, S. Yang, B. Shu, L. Chen, R. Yang, Y. Xu, J. Xie, X. Liu, S. Qi, *J. Invest. Dermatol.* **2021**, *141*, 1573.
[21] F. Paneni, S. Costantino, L. Castello, R. Battista, G. Capretti, S. Chiandotto, D. D'Amario, G. Scavone, A. Villano, A. Rustighi, F. Crea, D. Pitocco, G. Lanza, M. Volpe, G. Del Sal, T. F. Luscher, F. Cosentino, *Eur. Heart J.* **2015**, *36*, 817.
[22] A. P. Veith, K. Henderson, A. Spencer, A. D. Sligar, A. B. Baker, *Adv. Drug Delivery Rev.* **2019**, *146*, 97.
[23] J. Devalliere, K. Dooley, Y. Hu, S. S. Kelangi, B. E. Uygun, M. L. Yarmush, *Biomaterials* **2017**, *141*, 149.
[24] C. Niu, Z. Chen, K. T. Kim, J. Sun, M. Xue, G. Chen, S. Li, Y. Shen, Z. Zhu, X. Wang, J. Liang, C. Jiang, W. Cong, L. Jin, X. Li, *Autophagy* **2019**, *15*, 843.
[25] P. Zhao, B. D. Sui, N. Liu, Y. J. Lv, C. X. Zheng, Y. B. Lu, W. T. Huang, C. H. Zhou, J. Chen, D. L. Pang, D. D. Fei, K. Xuan, C. H. Hu, Y. Jin, *Aging Cell* **2017**, *16*, 1083.
[26] S. Das, G. Singh, A. B. Baker, *Biomaterials* **2014**, *35*, 196.
[27] M. C. Robson, T. A. Mustoe, T. K. Hunt, *Am. J. Surg.* **1998**, *176*, 80S.
[28] I. Papantoniou, G. Nilsson Hall, N. Loverdou, R. Lesage, T. Herpelinck, L. Mendes, L. Geris, *Adv. Drug Delivery Rev.* **2021**, *169*, 22.
[29] B. Tonnarelli, M. Centola, A. Barbero, R. Zeller, I. Martin, *Curr. Top. Dev. Biol.* **2014**, *108*, 319.
[30] M. Takeo, T. Tsuji, *Curr. Opin. Genet. Dev.* **2018**, *52*, 42.
[31] T. Mammoto, A. Mammoto, Y. S. Torisawa, T. Tat, A. Gibbs, R. Derda, R. Mannix, M. de Bruijn, C. W. Yung, D. Huh, D. E. Ingber, *Dev. Cell* **2011**, *21*, 758.
[32] T. Takebe, M. Enomura, E. Yoshizawa, M. Kimura, H. Koike, Y. Ueno, T. Matsuzaki, T. Yamazaki, T. Toyohara, K. Osafune, H. Nakauchi, H. Y. Yoshikawa, H. Taniguchi, *Cell Stem Cell* **2015**, *16*, 556.
[33] K.-W. Mok, N. Saxena, N. Heitman, L. Grisanti, D. Srivastava, M. J. Muraro, T. Jacob, R. Sennett, Z. Wang, Y. Su, L. M. Yang, A. Ma'ayan, D. M. Ornitz, M. Kasper, M. Rendl, *Dev. Cell* **2019**, *48*, 32.
[34] M. Yin, M. Pacifici, *Dev. Dyn.* **2001**, *222*, 522.
[35] A. M. McDermott, S. Herberg, D. E. Mason, J. M. Collins, H. B. Pearson, J. H. Dawahare, R. Tang, A. N. Patwa, M. W. Grinstaff, D. J. Kelly, E. Alsberg, J. D. Boerckel, *Sci. Transl. Med.* **2019**, *11*, aav7756.
[36] S. Herberg, A. M. McDermott, P. N. Dang, D. S. Alt, R. Tang, J. H. Dawahare, D. Varghai, J. Y. Shin, A. McMillan, A. D. Dikina, F. He, Y. B. Lee, Y. Cheng, K. Umemori, P. C. Wong, H. Park, J. D. Boerckel, E. Alsberg, *Sci. Adv.* **2019**, *5*, eaax2476.
[37] H. Chen, H. Fu, X. Wu, Y. Duan, S. Zhang, H. Hu, Y. Liao, T. Wang, Y. Yang, G. Chen, Z. Li, W. Tian, *Sci. Adv.* **2020**, *6*, eaay1514.
[38] K. Xuan, B. Li, H. Guo, W. Sun, X. Kou, X. He, Y. Zhang, J. Sun, A. Liu, L. Liao, S. Liu, W. Liu, C. H. Hu, S. Shi, Y. Jin, *Sci. Transl. Med.* **2018**, *10*, eaaf3227.
[39] H. Guo, B. Li, M. Wu, W. Zhao, X. He, B. Sui, Z. Dong, L. Wang, S. Shi, X. Huang, X. Liu, Z. Li, X. Guo, K. Xuan, Y. Jin, *Biomaterials* **2021**, *279*, 121223.
[40] B. D. Sui, B. Zhu, C. H. Hu, P. Zhao, Y. Jin, *Methods Mol. Biol.* **2019**, *2002*, 87.
[41] M. Wu, X. Liu, Z. Li, X. Huang, H. Guo, X. Guo, X. Yang, B. Li, K. Xuan, Y. Jin, *Cell Proliferation* **2021**, *54*, e13074.
[42] B. D. Sui, C. X. Zheng, W. M. Zhao, K. Xuan, B. Li, Y. Jin, *Physiol. Rev.* **2023**, https://doi.org/10.1152/physrev.00019.2022
[43] J. Liu, X. Qiu, Y. Lv, C. Zheng, Y. Dong, G. Dou, B. Zhu, A. Liu, W. Wang, J. Zhou, S. Liu, S. Liu, B. Gao, Y. Jin, *Stem Cell Res. Ther.* **2020**, *11*, 507.
[44] D. Chakroborty, S. Goswami, S. Basu, C. Sarkar, *FASEB J.* **2020**, *34*, 14093.
[45] G. Li, C. N. Ko, D. Li, C. Yang, W. Wang, G. J. Yang, C. Di Primo, V. K. W. Wong, Y. Xiang, Y. Lin, D. L. Ma, C. H. Leung, *Nat. Commun.* **2021**, *12*, 3363.
[46] J. Chaudhuri, Y. Bains, S. Guha, A. Kahn, D. Hall, N. Bose, A. Gugliucci, P. Kapahi, *Cell Metab.* **2018**, *28*, 337.
[47] M. A. Mengstie, E. C. Abebe, A. B. Teklemariam, A. T. Mulu, M. M. Agidew, M. T. Azezew, E. A. Zewde, A. A. Teshome, *Front. Mol. Biosci.* **2022**, *9*, 1002710.
[48] M. Yang, C. J. Li, X. Sun, Q. Guo, Y. Xiao, T. Su, M. L. Tu, H. Peng, Q. Lu, Q. Liu, H. B. He, T. J. Jiang, M. X. Lei, M. Wan, X. Cao, X. H. Luo, *Nat. Commun.* **2017**, *8*, 16003.
[49] J. C. Hu, C. X. Zheng, B. D. Sui, W. J. Liu, Y. Jin, *World J. Stem Cells* **2022**, *14*, 318.
[50] K. Zhang, L. Liu, K. Shi, K. Zhang, C. Zheng, Y. Jin, *Tissue Eng., Part C* **2022**, *28*, 393.
[51] C. L. Deng, C. B. Hu, S. T. Ling, N. Zhao, L. H. Bao, F. Zhou, Y. C. Xiong, T. Chen, B. D. Sui, X. R. Yu, C. H. Hu, *Cell Death Differ.* **2021**, *28*, 1041.
[52] S. J. Xing, K. C. Zhang, S. Y. Tang, L. Liu, Y. Cao, C. X. Zheng, B. D. Sui, Y. Jin, *J. Vis. Exp.* **2022**, *187*, e64135.
[53] C. O'Connor, E. Brady, Y. Zheng, E. Moore, K. R. Stevens, *Nat. Rev. Mater.* **2022**, *7*, 702.
[54] J. Zhang, J. Pan, W. Jing, *Cell Proliferation* **2020**, *53*, e12874.
[55] Y. Peng, S. Wu, S. Y. Li, J. L. Crane, *Theranostics* **2020**, *10*, 426.
[56] H. Xie, Z. Cui, L. Wang, Z. Xia, Y. Hu, L. Xian, C. Li, L. Xie, J. Crane, M. Wan, G. Zhen, Q. Bian, B. Yu, W. Chang, T. Qiu, M. Pickarski, L. T. Duong, J. J. Windle, X. Luo, E. Liao, X. Cao, *Nat. Med.* **2014**, *20*, 1270.
[57] R. Xu, A. Yallowitz, A. Qin, Z. Wu, D. Y. Shin, J. M. Kim, S. Debnath, G. Ji, M. P. Bostrom, X. Yang, C. Zhang, H. Dong, P. Kermani, S. Lalani, N. Li, Y. Liu, M. G. Poulos, A. Wach, Y. Zhang, K. Inoue, A. Di Lorenzo,

B. Zhao, J. M. Butler, J. H. Shim, L. H. Glimcher, M. B. Greenblatt, *Nat. Med.* **2018**, *24*, 823.

[58] L. Wang, F. Zhou, P. Zhang, H. Wang, Z. Qu, P. Jia, Z. Yao, G. Shen, G. Li, G. Zhao, J. Li, Y. Mao, Z. Xie, W. Xu, Y. Xu, Y. Xu, *Cell Death Dis.* **2017**, *8*, e2760.

[59] J. Chen, M. Li, A. Q. Liu, C. X. Zheng, L. H. Bao, K. Chen, X. L. Xu, J. T. Guan, M. Bai, T. Zhou, B. D. Sui, D. H. Li, Y. Jin, C. H. Hu, *Stem Cell Rep.* **2020**, *15*, 110.

[60] S. Maschalidi, P. Mehrotra, B. N. Keceli, H. K. L. De Cleene, K. Lecomte, R. Van der Cruyssen, P. Janssen, J. Pinney, G. van Loo, D. Elewaut, A. Massie, E. Hoste, K. S. Ravichandran, *Nature* **2022**, *606*, 776.

[61] P. K. Moulik, R. Mtonga, G. V. Gill, *Diabetes Care* **2003**, *26*, 491.

[62] C. Wetzler, H. Kämpfer, B. Stallmeyer, J. Pfeilschifter, S. Frank, *J. Invest. Dermatol.* **2000**, *115*, 245.

[63] L. K. Phng, H. Gerhardt, *Dev. Cell* **2009**, *16*, 196.

[64] A. P. Kusumbe, S. K. Ramasamy, T. Itkin, M. A. Mae, U. H. Langen, C. Betsholtz, T. Lapidot, R. H. Adams, *Nature* **2016**, *532*, 380.

[65] M. W. Hsieh, W. T. Wang, C. Y. Lin, Y. R. Kuo, S. S. Lee, M. F. Hou, Y. C. Wu, *Biomedicines* **2022**, *10*, 2085.

[66] N. Kosaric, H. Kiwanuka, G. C. Gurtner, *Expert Opin. Biol. Ther.* **2019**, *19*, 575.

[67] H. Cho, M. R. Blatchley, E. J. Duh, S. Gerecht, *Adv. Drug Delivery Rev.* **2019**, *146*, 267.

[68] J. Chen, C. X. Zheng, Y. Jin, C. H. Hu, *Stem Cells* **2021**, *39*, 838.

[69] M. Deptula, A. Brzezicka, A. Skoniecka, J. Zielinski, M. Pikula, *Med. Res. Rev.* **2021**, *41*, 2130.

[70] S. A. Mathew, C. Naik, P. A. Cahill, R. R. Bhonde, *Cell. Mol. Life Sci.* **2020**, *77*, 253.

[71] S. Kuang, F. He, G. Liu, X. Sun, J. Dai, A. Chi, Y. Tang, Z. Li, Y. Gao, C. Deng, Z. Lin, H. Xiao, M. Zhang, *Biomaterials* **2021**, *275*, 120963.

[72] S. Du, D. I. Zeugolis, T. O'Brien, *Stem Cell Res. Ther.* **2022**, *13*, 426.

[73] L. Cheng, A. F. Hill, *Nat. Rev. Drug Discovery* **2022**, *21*, 379.

[74] G. van Niel, D. R. F. Carter, A. Clayton, D. W. Lambert, G. Raposo, P. Vader, *Nat. Rev. Mol. Cell Biol.* **2022**, *23*, 369.

[75] E. R. Bray, R. S. Kirsner, E. V. Badiavas, *Cold Spring Harbor Perspect. Biol.* **2022**, *14*, a041227.

[76] K. S. Lee, J. Lee, H. K. Kim, S. H. Yeom, C. H. Woo, Y. J. Jung, Y. E. Yun, S. Y. Park, J. Han, E. Kim, J. H. Sul, J. M. Jung, J. H. Park, J. S. Choi, Y. W. Cho, D. G. Jo, *J. Extracell. Vesicles* **2021**, *10*, e12152.

[77] M. Nakazaki, T. Morita, K. L. Lankford, P. W. Askenase, J. D. Kocsis, *J. Extracell. Vesicles* **2021**, *10*, e12137.

[78] W. Liu, R. Gao, C. Yang, Z. Feng, W. Ou-Yang, X. Pan, P. Huang, C. Zhang, D. Kong, W. Wang, *Sci. Adv.* **2022**, *8*, eabn7006.

[79] T. J. Keane, C. M. Horejs, M. M. Stevens, *Adv. Drug Delivery Rev.* **2018**, *129*, 407.

[80] C. Zheng, B. Sui, X. Zhang, J. Hu, J. Chen, J. Liu, D. Wu, Q. Ye, L. Xiang, X. Qiu, S. Liu, Z. Deng, J. Zhou, S. Liu, S. Shi, Y. Jin, *J. Extracell. Vesicles* **2021**, *10*, e12109.

[81] S. A. Park, J. Covert, L. Teixeira, M. J. Motta, S. L. DeRemer, N. L. Abbott, R. Dubielzig, M. Schurr, R. R. Isseroff, J. F. McAnulty, C. J. Murphy, *Wound Repair Regener.* **2015**, *23*, 251.

[82] C. X. Zheng, J. Chen, J. Y. Tian, X. Y. Huang, Y. Jin, B. D. Sui, *STAR Protoc.* **2022**, *3*, 101674.

[83] X. Qiu, J. Liu, C. Zheng, Y. Su, L. Bao, B. Zhu, S. Liu, L. Wang, X. Wang, Y. Wang, W. Zhao, J. Zhou, Z. Deng, S. Liu, Y. Jin, *Cell Proliferation* **2020**, *53*, e12830.

[84] C. H. Hu, B. D. Sui, J. Liu, L. Dang, J. Chen, C. X. Zheng, S. Shi, N. Zhao, M. Y. Dang, X. N. He, L. Q. Zhang, P. P. Gao, N. Chen, H. J. Kuang, K. Chen, X. L. Xu, X. R. Yu, G. Zhang, Y. Jin, *Small Methods* **2022**, *6*, 2100763.